A Radiation Tolerant Optical Link for the Read–Out of the ATLAS LAr Calorimeter

Johan Lundquist

KUNGLIGA TEKNISKA HÖGSKOLAN

Stockholm 2000

A Radiation Tolerant Optical Link for the Read–Out of the ATLAS LAr Calorimeter

Johan Lundquist

AKADEMISK AVHANDLING

som med tillstånd av Kungl Tekniska Högskolan framlägges till
offentlig granskning för vinnande av teknologie licensiatexamen
måndagen den 5 juni 2000, kl. 11
i föreläsningssalen, Manne Sigbahnhuset KTH Frescati
Frscativägen 24, Stockholm

Avhandlingen försvaras på engelska

Kungl Tekniska Högskolan
Stockholm 2000

Johan Lundquist: A Radiation Tolerant Optical Link for the Read–Out of the ATLAS LAr Calorimeter

ABSTRACT

ATLAS is a large general purpose experiment which will be located at the Large Hadron Collider, LHC. The performance of candidate electronic and optoelectronic components for an 1.28 Gb/s radiation tolerant optical read–out link for the ATLAS liquid argon calorimeter system has been studied. A demonstrator optical link based around the use of the commercial G–link serialiser chipset, Vertical Cavity Surface Emitting Laser Diodes (VCSELs) and multimode optical fibres, has been built and tested in neutron and gamma radiation environments. The components have been found to be radiation tolerant up to at least a neutron fluence of 1.7×10^{13} n(1 MeV(Si))/cm^2 and an ionising dose of 800 Gy(Si). However, Single–Event Upsets (SEU) in the G–link serialiser chip were observed during neutron irradiations. An estimate of the expected ATLAS SEU rate, based on the the use of Burst Generation Rate curves for silicon has been performed and leads to an error rate prediction of 2±1errors every 100 hours of LHC running.

Descriptors: ATLAS, LHC, liquid argon calorimeter, radiation tolerance, optical link, SEU, VCSEL, optical fibre

ISBN 91-7170-587-2
Printed by Högskoletryckeriet KTH 2000

Table of Contents

1 INTRODUCTION

1.1 Outline of the Thesis 12

2 THE LHC AND ATLAS

2.1 The LHC 14

2.1.1 Magnets and RF–Cavities 14
2.1.2 Particle Production 16
2.1.3 Experiments 16

2.2 ATLAS 17

2.2.1 The Inner Detector 18
2.2.2 Calorimeters 20
2.2.3 Magnet System 21
2.2.4 Muon Spectrometer 21
2.2.5 The ATLAS Trigger 22

3 ATLAS LIQUID ARGON CALORIMETER SYSTEM

3.1 Introduction 24

3.2 LAr Sampling Calorimeters 24

3.2.1 Working Principle for EM Calorimeters 24
3.2.2 Energy Resolution 25
3.2.3 Jets and Hadronic Showers 25

3.3 ATLAS LAr Calorimeters 26

3.3.1 EM Calorimeters 26
3.3.2 Hadronic Calorimetry 28

3.4 LAr Electronics 29

3.4.1 Requirements 29
3.4.2 The Front End System 30
3.4.3 The Read Out Drivers 32

4 THE OPTICAL LINK

4.1 Why Optical links 34

4.2 Link Requirements 34

4.3 The Demonstrator Link 35

4.4 Key components 36

4.4.1 VCSELs 36
4.4.2 Optical Fibres 37
4.4.3 Transceivers 39
4.4.4 PIN–diodes 39
4.4.5 The G–link Serialiser 39

5 RADIATION ISSUES

Table of Contents

5.1 Radiation Environment in ATLAS 42

5.1.1 Simulations 43

5.2 Particle Interactions 45

5.2.1 Ionising Interactions 45
5.2.2 Non–Ionising Interactions 47

5.3 Displacement Damage in Semiconductors 47

5.3.1 General Considerations 47
5.3.2 Annealing 49
5.3.3 Displacement Damage in GaAs VCSELs 49
5.3.4 Displacement Damage in Bipolar IC circuits 49

5.4 Radiation Effects in Optical Fibres 50

5.5 Single–Event Effects 50

5.5.1 Single Event Upset 51
5.5.2 Neutron Induced SEUs 52
5.5.3 Single–Event Latchup 54
5.5.4 Single–Event Burnout 55

6 TOTAL DOSE STUDIES

6.1 Introduction 56

6.2 Test Facilities 56

6.2.1 Neutron Irradiation 56
6.2.2 Gamma Irradiation 58

6.3 VCSEL irradiation 59

6.3.1 Experimental Procedure 59
6.3.2 Irradiation Details 60
6.3.3 Results 61

6.4 Fibre Irradiation 62

6.4.1 Experimental Procedure 62
6.4.2 Irradiation Details 62
6.4.3 Results 63

6.5 Performance of the Transceivers 64

6.6 G–link Irradiation 65

6.6.1 Experimental Procedure 65
6.6.2 Results 65

7 SEU TESTS OF THE DEMONSTRATOR LINK

7.1 Experimental Procedure 66

7.1.1 General Description 66
7.1.2 Radiation Environment 67

7.2 Results 68

Table of Contents

7.2.1 Error Types 68
7.2.2 Measured Error Rates 70
7.2.3 BGR Analysis 70

8 SUMMARY AND OUTLOOK

8.1 Total Dose Studies of Single Components 74

8.1.1 VCSELs 74
8.1.2 Fibres 74
8.1.3 Transceivers 74
8.1.4 G–link Serialiser 75

8.2 SEU Studies of the G–link 75

8.3 Outlook 75

9 ACKNOWLEDGEMENTS

BIBLIOGRAPHY

INTRODUCTION 11

THE LHC AND ATLAS 14

The Large Hadron Collider and the four experiments, ATLAS, CMS, ALICE and LHC–b, situated along it. 14
A cross–section of the LHC dipole bending magnets. 15
Particle production cross–sections in p–p collisions as a function of $\sqrt{s}$ [7]. *16*
The ATLAS detector system. 17
The ATLAS Inner Detector system. SCT stands for "SemiConductor Tracker" and TRT for "Transition Radiation Tracker". 19
The ATLAS calorimeter system. 20
The ATLAS Muon System (barrel part) 21
The ATLAS 3–level trigger 22

ATLAS LIQUID ARGON CALORIMETER SYSTEM 24

Principle of a sampling calorimeter 24
The ATLAS LAr–calorimeter system. 26
a) The accordion shaped absorber in the barrel EM calorimeter b) A simulation of an electromagnetic shower in the barrel EM calorimeter. 27
The front face of an EM FCAL module. R_M indicates the "Molière radius". The shower is roughly contained in a cylinder with the radius $2R_M$. 29
Signal shape as produced in the detector (triangle), 29
The LAr electronic system. 31
Signal shape as produced in the detector (triangle), and after shaping (curve with dots). The dots represents the different samplings. 32
The structure of the 32–bit data words that will be transmitted over the LAr optical link. One of these events contains information about energy and gain from 128 calorimeter cells (one FEB). 33

THE OPTICAL LINK 34

A Gb/s demonstrator link based on the G–link chipset. In the figure a scheme for multiplexing the 32 bit data to fit the 16 bit structure of the G–link is also shown. However, this has never been implemented in any of the tests described in the following chapters. Without this multiplexing every 16 bit data word is sent twice, given a frequency of 40 MHz. In the final link solution a multiplexer will be built in a radiation hard DMILL technology [21]. 36
Schematic of a VCSEL. 37
Characteristics of a typical VCSEL. 38
Graded index fibre (GRIN) , (left) profile of the refraction index as function of radius.(middle) fibre cross section (right) light ray paths in the fibre [25]. 39
(left) A VCSEL in a TO–46 package. 40
(right) A transceiver module with two SC–connectors. 40
The structure of the serial data and the fill frames for the G–link. The "master transition" is used by the Rx for frequency locking. 40

RADIATION ISSUES 42

The ATLAS neutron spectrum. The bump at 10 MeV is an unexplained artifact from the simulations. 43
The importance of the three different photon interactions for different atomic number Z as a function of photon energy. The solid lines indicates the energy where the interactions on both sides of it are equally probable to take place and the dashed line indicates Si (Z=14) . 45
Energy dependence of the total stopping power and range for alpha particles incident on GaAs [31]. 46
Three effects that can occur due to the presence of defect centres in the silicon bandgap [31]. 48
Coloration in a Germanium doped silica fibre [34]. 50
The charge collection mechanism that cause single–event upsets [31]. 51
BGR curves for the six nuclear processes believed to be of most importance for the generation of SEUs in silicon [38]. 53
Three BGR curves plotted as a function of neutron energy. These are overlaid by the simulated ATLAS neutron spectrum and the spectrum obtained when a 26 MeV deuterium beam is collided with a Beryllium target. The ATLAS spectrum appears not to be normalised when compared to the other one, but this is an artifact of the y–axis cut–off at 0.12 above which the spectrum rises extremely steeply. 54

TOTAL DOSE STUDIES 56

a) The neutron spectrum at SARA. The method used to measure this spectrum a is based on a TOF technique, where NE213 scintillators were used. This introduce a cutoff at around 1MeV [40].
b) Neutron Yield for the $^{9}Be(d,n)^{10}B$ reaction in a “thick” beryllium target as a function of deuterium energy. 57
Neutron spectra for deuterium with different energies impinging on a beryllium target [44]. 58
a) The target area at the CERI neutron irradiation facility. b) The ^{60}Co source at Karolinska hospital. 59
The FR4 motherboard with four Honeywell and 5 Mitel VCSELs in ST housings. 60

a) Relative attenuation of the light output from a typical Honeywell VCSEL as a function of the time during a neutron irradiation. Note the annealing behaviour after the irradiation is completed.
b) Relative attenuation of the light output from a typical Mitel VCSEL as a function of the time during a gamma irradiation. Note the absence of annealing after the irradiation is completed. The dotted line denotes a 10 year LHC equivalent dose. The two atypical points seen in the annealing phase are spurious. 61

a) The induced loss in the POF and Acome-supplied fibres as a function of neutron fluence. The POF(Ljub) measurements come from a test done by others [4]. For the POF fibres the points with the smaller error bars correspond to the longer length of fibre tested.
b) The induced loss in the POF and Acome–supplied fibres as a function of ionising dose. The POF measurements come from four independent tests done by others [4]
c) The light power throughput in an Acome fibre during exposure to neutron irradiation. After the end of the irradiation the fibre is seen to anneal.
d) The light power throughput in an Acome fibre during exposure to gamma irradiation. No evidence of annealing is seen after the end of the irradiation. 64

SEU TESTS OF THE DEMONSTRATOR LINK 66

The demonstrator link in a typical test beam setup. 67
The measured error rate at a fixed deuteron beam energy (20MeV) as a function of the incident deuteron beam current (which is proportional to the neutron flux measured at SARA). 70
The distribution of link–down times measured at CERI. 70
The measured error rate at a nominal flux of 3×10^{7} $ncm^{-2}s^{-1}$, as a function of deuterium energy. The different shading indicates the fraction of the different error types: data, error flag and linkready flag. 71
The transient error rate overlaid with the BGR convolution integrals. 72

SUMMARY AND OUTLOOK 74

ACKNOWLEDGEMENTS 77

CHAPTER 1

INTRODUCTION

The science of high energy particles and their interaction with matter began with the discovery in November 1895 of X-rays by William Röntgen [1]. Less than a month later in early 1896 Becquerel noticed that his photographic plates became fogged and thereby discovered radioactivity. In 1897 J.J. Thomson discovered the electron and a year later in 1898 Marie Curie isolated radium. Thus only a century ago nuclear and particle physics was born.

Since the 1890s, many people have worked hard trying to understand the new world of phenomena that was discovered. When eventually succeeding in doing so, other people discovered new phenomena, making life less easy (but more interesting ?) for the ones who thought they had understood the old phenomena. As it has turned out, this way of questioning old theories with the support of new observations and subsequently redefining the theories (sometimes leading to predictions of yet undiscovered phenomena) has been very successful. Following this path has led us to the current theoretical description of the elementary building blocks of matter which is called the Standard Model. This theory describes how the basic constituents of matter - leptons and quarks - interact via the exchange of gauge bosons. These bosons are massless gluons mediating strong interactions, massless photons mediating electromagnetic interactions, and massive W and Z bosons associated with weak interactions. Earlier theories predicted a symmetry between the photon and the W and Z bosons predicting that they all should have zero rest mass. In nature, however, the symmetry is broken. The photon remains massless but the W and Z bosons acquire a significant mass of ~80 GeV and ~91 GeV respectively. This symmetry breaking mechanism must be associated with the existence of new physical phenomena. However, these new effects are expected to be insignificant at low energies, but should become evident at an energy scale of about 1 TeV.

This is the main reason why the LHC (Large Hadron Collider) project was born. The LHC is the next big accelerator currently being built at CERN. It is an accelerator that is designed to collide bunches of protons at a centre of mass energy of 14 TeV at a rate of about 40 MHz. One of the experiments situated along the LHC is called ATLAS. An important part of the ATLAS detector is the liquid argon calorimeter system based upon the use of liquid argon detectors for detecting and measuring the energy of the particles created in the proton–proton collisions. The entire calorimeter system has ~200 000 electronics channels. Information from these must be transferred over a data link, away from the detector to the data acquisition system. This is located in an adjacent underground cavern or in surface buildings, requiring data transmission over distances of 100 to 200 m.

At present particle physics experiments, data is primarily being transferred off–detector by copper cables. The large number of links, needed in ATLAS to transfer data from all channels, makes the use of copper cables undesirable due to their large volume and density which would interfere with particle detection. It is also expected that copper cables would lead to problems with ground loops generated by the shielded cables connected to the detector. Non–metallic optical links allow detector subsystems to be decoupled from off–detector electronics, reducing coherent noise problems from ground loops. An unusual constraint on the optical links is that the optoelectronic components and fibre in the vicinity of the detec-

tor must withstand high levels of neutron and ionising radiation.

The theories for radiation damage of semiconductive materials arose in the late 1950s, as it was an urgent need to understand why semiconductive devices used in space and military equipment often were left “stone dead” after exposure to the space environment or in the vincinity of nuclear explosions. Another issue was first postulated by Wallmark and Marcus in 1962 [2]. This was the possibility of Single–Event Effects (SEE), where a single energetic charged particle causes an alteration in the logical state at a device node.

The work in this thesis centres around tests performed to gain understanding of how the radiation environment in the ATLAS detector will effect the components of the optical read–out link for the liquid argon calorimeter system. All radiation tests has been conducted in cooperation with three other institutes ISN[†] in Grenoble, CPPM[‡] in Marseille and SMU[§] in Dallas.

1.1 Outline of the Thesis

In Chapter 2 The LHC collider will be described briefly as well as the experiment that this work focuses on – ATLAS.

In Chapter 3 the liquid argon calorimeter system is described. This system includes a barrel region, composed of an EM calorimeter combined with an active presampling layer, and an end–cap region with three different detectors; one electromagnetic with presampler one hadronic and one forward calorimeter. Also described is the front–end read–out electronics, which is based on the same technique for all LAr calorimeters.

A radiation tolerant optical link is used to transfer data from the front–end boards to remote read–out drivers located up to 200 m away. The LAr optical link will be composed of a serialiser, an optical transmitter (a Vertical Cavity Surface Emitting Laser diode, VCSEL, and supporting electronics in this case), an optical channel (a fibre), and an optical receiver (a PIN–diode and supporting electronics) with associated optical and electrical connectors. In Chapter 4 a demonstrator link composed of these components is described.

The basic mechanisms of radiation effects on electronics are reviewed in Chapter 5. Topics discussed include the effects of displacement damage and ionizing radiation, single–event phenomena and radiation effects on VCSELs, fibres and Integrated circuits. A method for evaluating the rate at which neutron induced single–event upsets (SEU) occur, given the neutron energy spectrum, is also presented.

In Chapter 6 a series of total dose radiation tests with neutron and gamma radiation, performed at a few different locations in Sweden and France, are described. The induced attenuation of VCSELs and optical fibres have been measured along with functional tests of the G–link seialiser chip. The results presented in this chapter are summarised in two papers submitted to Nucl. Instr. and Meth. A [3], [4]

When performing the neutron total dose studies of the G–link, SEUs were observed. This behaviour required further testing. Three neutron irradiation tests of the demonstrator link were performed are summarised in Chapter 7. The SEU rate dependence on flux and neutron energy was measured. The aim was to infer the SEU rate in ATLAS. The results presented

† Insitute des Sciences Nucléaires
‡ Centre De Physique Des Partiques De Marseille
§ Southern Methodist University

in this chapter are summarised in a paper submitted to Nucl. Instr. and Meth. A [5].

The final chapter contains a concise summary of the work presented in this thesis together with an outlook.

CHAPTER 2

THE LHC AND ATLAS

The LHC collider is the next big accelerator project at CERN, the European Laboratory for High Energy Physics. The LHC will collide two counter–rotating beams of protons at energies higher than ever achieved before. The accelerator will be briefly described in this chapter as well as the experiment that this work focuses on – ATLAS.

2.1 The LHC

LHC [6] will start to operate in 2005. When installed in the 26.7km long tunnel at CERN, where the LEP accelerator now resides, the LHC will be capable of accelerating two beams of protons to a nominal energy of 7TeV per beam, which gives a total energy of 14TeV in centre of mass†. In addition to this, the accelerator will be able to run as a heavy ion collider (Pb–Pb) with a centre of mass energy of 1150TeV.

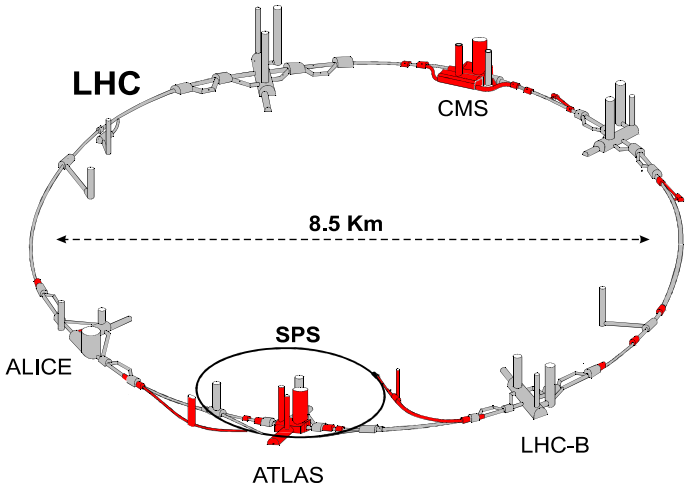

Figure 2-1: The Large Hadron Collider and the four experiments, ATLAS, CMS, ALICE and LHC–b, situated along it.

2.1.1 Magnets and RF–Cavities

In order to bend 7TeV protons around the ring, which radius is determined by the existing LEP–tunnel, the dipole bending magnets must be able to produce fields of 8.3T‡. To meet this requirement the magnets are superconducting (cooled with superfluid Helium). The coils in these 14.2m long magnets are made of copper clad niobium–titanium cables, a technology first used in a superconducting accelerator at the Fermilab Tevatron. The operating temperature will be 1.9K above absolute zero, an unusually low temperature that puts new demands on cable quality and coil–assembly. In all, 1296 of these dipole magnets will be

† A quick calculation shows that the velocity of the protons is the speed of light minus 3m/s.
‡ This is almost 100.000 times the earth's magnetic field.

required for LHC. In addition there will be a number of 3.1 m, 6.9 T superconducting quadrupole magnets for beam focusing.

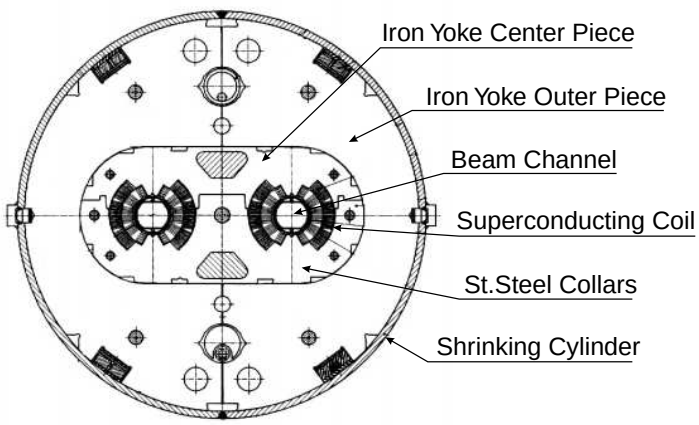

Figure 2-2: A cross–section of the LHC dipole bending magnets.

In order to maintain high luminosity, degradation of the beam caused by the beam crossing angle must me kept to a minimum. A crucial parameter which affects this is the longitudinal length of the particle bunches, which must be kept short. This is obtained with 16 MV RF cavities operating at 400 MHz. Each beam has a separate RF system composed of eight cavities. There will be ~2800 particle bunches, containing ~10^{11} protons each. The time interval between each bunch crossing is 25 ns which corresponds to a bunch crossing frequency of 40 MHz†. In Table 2-1 some of the most important LHC parameters are listed.

Parameter	**Value**
Energy at injection (per beam)	450 GeV
Energy at collision (centre of mass)	14 TeV
Dipole field at 7 TeV	8.33 T
Luminosity (low period)	10^{33} cm^{-2} s^{-1}
Luminosity (high period)	10^{34} cm^{-2} s^{-1}
Current per beam	0.56 A
Number of bunches	2835
Bunch separation	24.95 ns
Number of particles per bunch	1.1x10^{11}
Luminosity lifetime	10 h
Energy loss per turn per beam	6.7 keV
Total radiated power per beam and revolution	3.8 kW

Table 2-1: General LHC parameters.

† The exact values are actually 24.95 ns and 40.08 MHz.

2.1.2 Particle Production

In Figure 2-3 [7] some important production cross sections and interaction rates are shown as function of the centre of mass energy. The total cross section at LHC is subject to large uncertainties†. Depending on the theoretical model, the total cross section σ_{tot} is estimated to be between 90 and 130 mb. As a comparison, the cross–section for Higgs–production (m_{Higgs}=500GeV) is 11 orders of magnitude lower. Calculations have shown that, in order to produce enough Higgs–events above the QCD background during 10 years of LHC running, the luminosity must be of the order $10^{34}cm^{-2}s^{-1}$, a value that will be achieved after an initial 3 year period of running at the lower luminosity $10^{33}cm^{-2}s^{-1}$. This can be compared to the luminosity at present colliders, which culminates around $10^{32}cm^{-2}s^{-1}$. The right scale in Figure 2-3 shows the number of events produced at the luminosity $10^{34}cm^{-2}s^{-1}$.

At the higher luminosity, there will be on average 23 inelastic p–p interactions per bunch crossing. This means that, every 25 ns, about 2000 particles radiate from the interaction point into the surrounding detector (~10^{12} particles per second). With an average number of 30 charged particle tracks per interaction this results in approximately 750 charged tracks in the detectors every bunch crossing. This enormous production rate and particle multiplicity puts very high demands on the detectors and their read out electronics when it comes to speed and radiation hardness.

Luminosity

The luminosity L is approximated by:

$$L = fn\frac{N^2}{A}$$

were f denotes the revolution frequency, n is the number of bunches, N is the number of particles in each bunch and A is cross sectional area of the beam

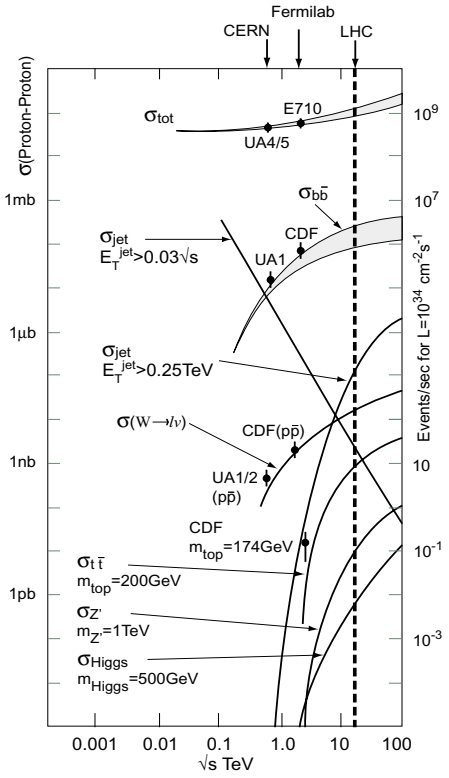

Figure 2-3: Particle production cross–sections in p–p collisions as a function of √s [7].

2.1.3 Experiments

There are four interaction points at LHC. All of them will be surrounded by experiments. Two are called ATLAS and CMS [8]. They are general purpose p–p experiments designed to detect as much as possible of the expected physics at LHC. The two other experiments, LHC–b [9] and ALICE [10], will be dedicated to research in B–physics and heavy ion physics respectively. This thesis focuses on the ATLAS detector which is described in the following section.

† The total cross section is extrapolated from experiments at earlier colliders like the UA4/5 (SPS) and E710 (Tevatron), while the theoretical uncertainties of the behaviour of σ_{tot} are large.

2.2 ATLAS†

Perhaps the most important aim for ATLAS is the search for the Higgs–boson, which is the only field quanta of the Standard Model yet to be experimentally verified. It is included in the theory to explain the origin of the spontaneous symmetry–breaking in the electroweak sector ($SU(2)\times U(1)$) [12]. This symmetry–breaking mechanism ("Higgs mechanism") is closely connected to one of the most fundamental questions in physics today: What is the origin of the different particle masses ?

Other activities are searches for supersymmetric particles, compositeness of the "fundamental" fermions, investigation of CP violation in b–decays and detailed studies of the top quark. Thus, the goal is to build a general purpose p–p detector, sensitive to the largest possible Higgs mass range, with ability to perform electron–, gamma–, muon– and jet–measurements to a high accuracy. Missing transverse energy measurements are important since this phenomena is a key signature for new physics like supersymmetry. Precision b–quark tagging is required to analyse events like $H \rightarrow b\bar{b}$, t–quarks decaying to b–quarks and also for studies of CP–violation.

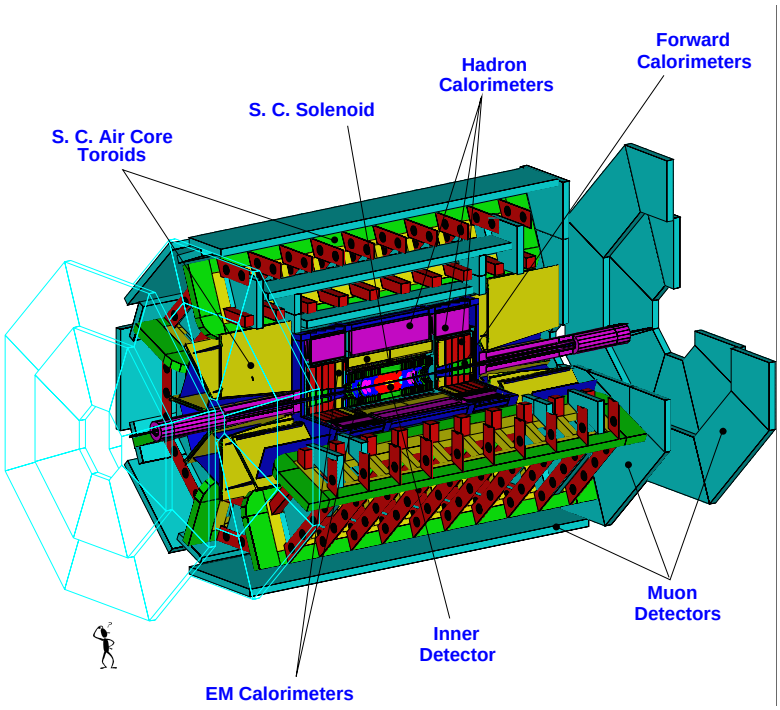

Figure 2-4: The ATLAS detector system.

Extreme demands are put on the ATLAS detector by the very high energy and luminosity at which LHC will operate (see Chapter 2.1), and by the need for highly granular sub–detectors due to the enormous particle multiplicity. ATLAS will have to be able to process a

† ATLAS is an abbreviation for *A Toroidal LHC ApparatuS*. A full description can be found in the ATLAS Technical Proposal [11].

vast amount of information, over a large dynamic range (a few GeV to about 3 TeV for the electromagnetic calorimeter†), at the LHC bunch crossing rate of 40 MHz. Furthermore, all detectors will suffer from both ionising and neutron irradiation. As an extreme example, the innermost detector components must be able to withstand ionising radiation doses up to 500 kGy and a neutron fluence of 10^{15}cm^{-2} over a period of 10 years [13]. ATLAS is optimized to operate at the highest luminosity while maintaining a good performance at the lower initial luminosity.

The detector structure chosen by the ATLAS collaboration to meet these requirements is the following (see Figure 2-4):

- A tracking system (Inner Detector), surrounded by a superconducting solenoid, to provide momenta measurements, charge and particle identification.
- Two calorimeter layers, one electromagnetic (EM) and one hadronic, to help reconstructing jets and perform precise measurements of particle/jet energies. In front of the EM calorimeters there is an additional "presampler" layer to sample early shower development in the Inner Detector and the solenoid.
- A muon system for muon momenta measurements that consists of a toroidal magnet system and muon detectors.

2.2.1 The Inner Detector

The Inner Detector [14] is located closest to the beam pipe, inside all of the other detectors. It consists of three sub–detectors, a *silicon pixel detector*, a *silicon strip detector*, and a *transition radiation tracker*. A superconducting solenoid magnet giving an axial magnetic field of 2 T, which provides the possibility to do momentum measurements of charged particles, surrounds the Inner Detector. The Inner Detector performs high resolution position measurements of charged particles. It's primary tasks are:

- To help perform separation between electrons and photons (which is difficult to do in the electromagnetic calorimeter because of the very similar showers they produce there).
- To separate between electrons and pions.
- To identify b–hadrons and τ–leptons by tagging secondary vertices from the their decays.

The construction of the Inner Detector is a fine balance between the need for precise track reconstruction and the limited amount of material it can contain to prevent early shower development that would deteriorate energy measurements in the calorimeters.

The Silicon Pixel Detector

The pixel detector must be able to resolve secondary vertices from short lived particles like b–hadrons and τ–leptons. The barrel part of the detector consists of three layers of silicon–semiconductor sensors lying at approx. 4, 10 and 14 cm from the interaction point. The sensor is a 16×60 mm wafer with over half a million pixels, 50×300 µm each. A Pixel module is composed of 16 bare front–end chips bonded to a sensor substrate. There are 2228 modules, in a cylinder 1.6 m long, 0.5 m in diameter centred on the interaction point, read out on 140 million channels.

The front–end chips are critical heat sources (0.6 W/cm^2) radiating more than 14 kW in the

† The lower limit is set by semi–leptonic decays like b→c e ν, and the upper by the decay of heavy gauge bosons (Z' and W'), predicted by some theoretical models.

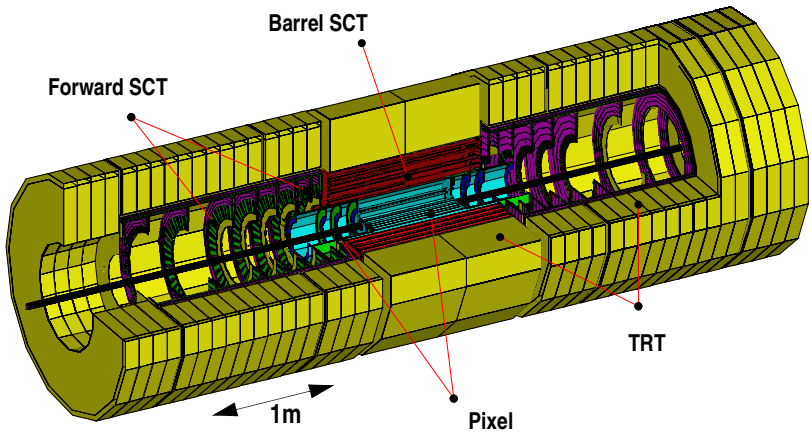

Figure 2-5: The ATLAS Inner Detector system. SCT stands for "SemiConductor Tracker" and TRT for "Transition Radiation Tracker".

detector volume. This heat is taken out via integrated cooling channels in the detector support elements.

The SemiConductor Tracker (SCT)

To allow for additional position measurements further from the interaction point (30–52 cm in the barrel region), a semiconductor tracker composed of four additional layers of silicon segmented in narrow strips is used. The strips are about 80 µm wide and several cm long. Each layer has a stereographical structure which means that there are two sets of strips, running at an angle of 2.3° relative to each other. On the barrel cylinders, the strips run parallel to the beam axis. On the end–cap disks, they run radially. The reason for not using additional pixel detectors at this radius is purely economical.

The Transition–Radiation Tracker (TRT)

At larger radii, it becomes too expensive to cover the required area with silicon strip detectors. Instead a technique based on transition–radiation trackers has been chosen. These are gas–wire drift detectors that consist of 4 mm thick tubes ("straws") embedded in a foam that contains lots of transitions between media of different dielectric constants. A charged particle traversing the foam radiate soft X–rays at each transition. Thin wires run through the tube centres. The tubes are filled mainly with Xenon, which is a good X–ray absorber. High voltage is applied between the wire and the metallised tube wall. When a particle with a sufficiently high γ factor traverses the detector, the X–rays produced in the transition medium, are converted into electrons by the Xenon inside the tubes. These electrons causes the wire to produce a discharge that, through accurate timing, determines how far from the wire the particle passed. With the large number of ~35 tracking points per track, a continous track with a resolution of 170 µm per straw is obtained. Moreover, The TRT allows for the possibility to distinguish between particles with a γ–factor above and below 10^3.

ATLAS coordinates

ATLAS has a cylidrical symmetry. It would therefore seem intuitive to use the cylindrical coordinates r, z and ϕ, but instead, z, ϕ and the "pseudo rapidity" (η), defined as:

$$\eta = -\ln\tan(\theta/2)$$

are used. η is zero at $\theta = 90°$ and becomes infinite as θ goes to zero, close to the beam axis. This unit is practical since it's a good approximation of the Lorentz–invariant quantity "rapidity", and since particle distributions become relatively flat when plotted against it.

It consequently has the ability to separate between electrons and pions in the range 0.5–200 GeV.

2.2.2 Calorimeters

Most of the calorimeters in ATLAS use liquid argon (LAr) as their active medium. The only calorimeter that isn't based on LAr–technique is the barrel hadron calorimeter (Tilecal) which is briefly described below. Since the work in this thesis is relevant to the read–out of the LAr calorimeters, Chapter 3 is dedicated to a more detailed description of these.

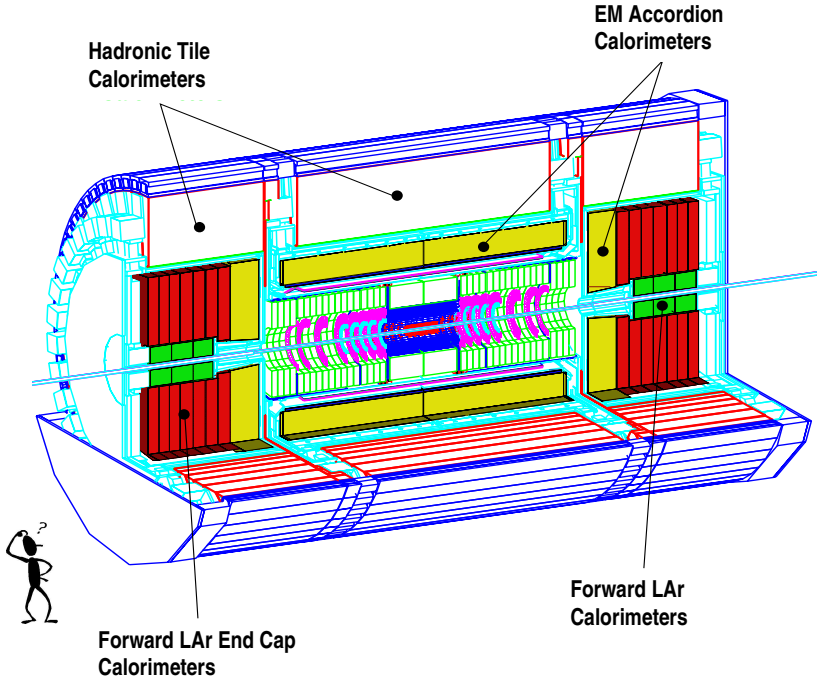

Figure 2-6: The ATLAS calorimeter system.

The Barrel Hadron Calorimeter (Tilecal)

Tilecal is a scintillating tile hadronic calorimeter [15]. The technology is based on a sampling technique using steel absorber material and scintillating tiles, read out by wavelength shifting (WLS) fibres. An innovative feature of this design is the orientation of the scintillating tiles which are placed in planes perpendicular to the colliding beams and staggered in depth. This orientation, verified by Monte Carlo simulations and beam tests of prototypes, provides good sampling homogeneity when placed behind the EM–calorimeter which presents about two interaction lengths of material in total. The tile calorimeter consists of a cylindrical structure with an inner radius of 2280 mm and an outer radius of 4230 mm. It is divided into a 5640 mm long central barrel and two 2650 mm long extended barrels. Each of them is further divided into 64 independent azimuthal modules.

The scintillator tiles lie in the r–ϕ plane and span the width of the module in the ϕ direction. WLS fibres running radially collect light from the tiles at both of their open edges. Read–

out cells are then defined by grouping together a set of fibres onto a photomultiplier, to obtain three dimensional segmentation. Radially, the calorimeter is segmented into three layers, approximately 1.5, 4.2 and 1.9 interaction lengths thick at η=0. The η–ϕ segmentation is 0.1×0.1 (0.2×0.1 in the last radial layer, the tail catcher).

2.2.3 Magnet System

The ATLAS magnet system consists of a barrel solenoid and air–core toroids. The 2 T solenoid is located in front of the barrel EM–calorimeter. The coil thickness has been minimized to avoid degradation of the EM–calorimeter performance. Also for this reason, the solenoid and the LAr barrel calorimeter shares the same cryostat, an arrangement that eliminates the material and space of independent container walls. The superconducting coil is composed of a single wire layer on the inside of a 5.3 m long support cylinder, with a winding radius of 1.22 m. The coil plus cryostat in front of the EM–calorimeter contributes 0.83 radiation lengths[†] (X_0) at normal incidence.

The superconducting air–core toroid magnet system is a part of the muon spectrometer, described below. It consists of a 26 m long barrel part with an inner bore of 9.4 m and an outer diameter of 19.5 m, and two end–caps with lengths 5.6 m and inner bores of 1.26 m, inserted at each end of the barrel. Both the end–cap and the barrel toroid is composed of eight flat coils symmetrically arranged about the beam axis, with the end–caps rotated with respect to the barrel so that the coils interleave.

2.2.4 Muon Spectrometer

One of the most important design criteria for ATLAS has been the quality of the muon measurements. One reason for this is that good muon momentum measurements are essential for identifying Higgs–decays such as $H \rightarrow ZZ \rightarrow ll\mu\mu$, where l can be any kind of lepton.

The muon system [16], illustrated in Figure 2-7, is composed of the superconducting toroidal magnets described above, and tracking detectors (muon chambers) with 60 μm intrinsic resolution. These detectors combine several different technologies; monitored drift tube chambers, cathode strip chambers, resistive plate chambers and thin gap chambers. For a detailed description of these, see [16]. The choice of chamber technology varies with η and depends primarily on the rate capability and spatial resolution of each technology.

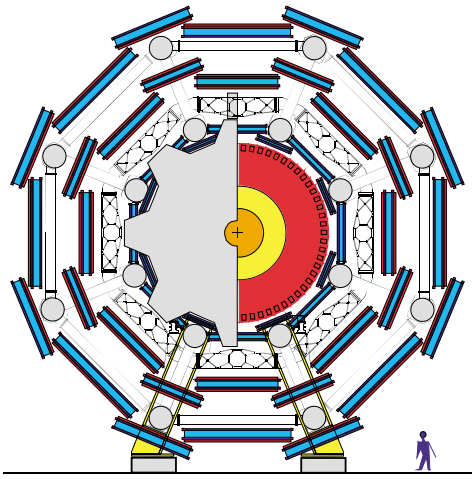

Figure 2-7: The ATLAS Muon System (barrel part)

The muon chamber planes are attached to the toroids to measure the muon trajectories. In

† A radiation length is defined as the average distance over which an electron loses 1–1/e (~63%) of it's energy due to bremsstrahlung.

the barrel, the layout consists of two layers of chambers at the inner and outer ends of the magnetic field volume plus an additional middle layer to measure the sagitta. In the forward direction the chambers are placed at the front and back of the toroid cryostats (see Figure 2-4), A third layer is situated against the cavern wall. This is to maximize the lever–arm of the point–angle measurement. The chambers are complemented with an independent fast trigger chamber system.

The muon system gives ATLAS it's overall dimensions. The outer chambers in the barrel are at a radius of about 11 m. The length of the barrel toroid coils are ±13 m, and the third layer of the forward muon chambers (mounted on the cavern wall) is located at ±21 m.

2.2.5 The ATLAS Trigger

The estimated maximum rate at which data can be recorded on permanent storage media in 2005 is ~100 Mb/s. Hence, it isn't possible to store the data from every reaction that takes place every 25 ns. Therefore one needs a "trigger" to select only those events that contains interesting physics. The ATLAS trigger is organized in three trigger levels (LVL1, LVL2, LVL3), as shown in Figure 2-8.

At LVL1 [17], specially designed processors accept data at the LHC bunch–crossing rate of 40 MHz. This data is low–granularity data from the calorimeters and the muon tracking, which means that the information in the single smallest detector cells has been clustered into larger groups. The LVL1 trigger is used to identify regions in the detector that contains interesting properties ("Regions of Interest") such as high missing p_T, EM clusters (electrons/photons), jets and muons. The trigger latency (time taken to take and report the LVL1 trigger decision) is ~2 μs (during which time detector data is buffered) and the maximum output rate is limited to 100 kHz by the capacities of the sub–detector read–out systems and the LVL2 trigger. As mentioned earlier, at high luminosity, each bunch crossing contains an average of about 23 p–p collisions. The LVL1 trigger must therefore select one interaction in ~10^4 (one bunch crossing in 400).

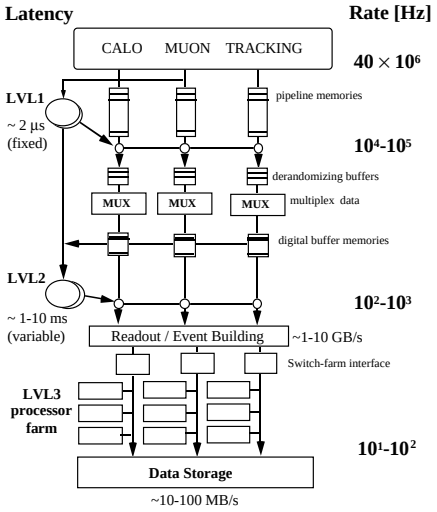

Figure 2-8: The ATLAS 3–level trigger

The LVL2 trigger design is based on the use of the "Regions of Interest" defined by LVL1. It then has to access and process only a small fraction of the total data. The LVL2 trigger processes full–granularity data from the Inner Detector, calorimeters and muon detectors, to find tracks and measure their p_T. The LVL2 trigger lowers the rate from ~100 kHz after LVL1 to ~1 kHz.

LVL1 and LVL2 are "hardware" triggers in the sense that they are composed of dedicated electronics[†]. LVL3 is a software trigger that use ordinary computers to make decisions. When an event is accepted by the LVL2 trigger, the data is sent to the LVL3 computer–farm

via the so called event builder. Complete event reconstruction is possible at LVL3, with decision times up to ~1 s. The system must accomplish a data–storage rate of 10–100 Mb/s by reducing the event rate and/or the event size. For some events, for example Higgs boson candidates, the full event data will be recorded with an event size of ~1 Mb, allowing a maximum event rate of ~100 Hz.

–♦–

† LVL1 uses custom electronics, whilst LVL2 uses commercial.

CHAPTER 3

ATLAS LIQUID ARGON CALORIMETER SYSTEM

In this chapter the liquid argon calorimeter system in ATLAS is described. This system includes a barrel region, composed of an EM calorimeter combined with an active presampling layer, and an end–cap region with three different detectors; one electromagnetic (+presampler), one hadronic and one forward. Also described is the front–end read–out electronics, which is based on the same technique for all LAr calorimeters. The optical read–out link is briefly described in the last section.

3.1 Introduction

The purpose of a calorimeter is to measure the energy of single particles and jets by absorbing the incident particles and subsequently transforming their initial energy to electric pulses. Unlike other devices used for energy measurements like magnetic spectrometers, the size of a calorimeter increases logarithmically with energy. This means that a relatively compact detector is able to measure very high energies. Calorimeters are sensitive to neutral as well as charged particles.

3.2 LAr Sampling Calorimeters

The Liquid Argon (LAr) calorimeters [18] in ATLAS are so–called “sampling calorimeters”. This means that they are composed of alternating layers of absorbers and sensing devices.

3.2.1 Working Principle for EM Calorimeters

Electrons and photons with energy above 100 MeV entering a medium, loses energy primarily by bremsstrahlung and pair production respectively. Thus, when such a photon or electron enters the calorimeter an electron–photon shower is initiated in the absorber material in the following way: A high energy electron radiates a photon by brehmsstrahlung. This photon then converts into an electron positron pair of which both will radiate photons that will decay into more electron positron pairs etc.

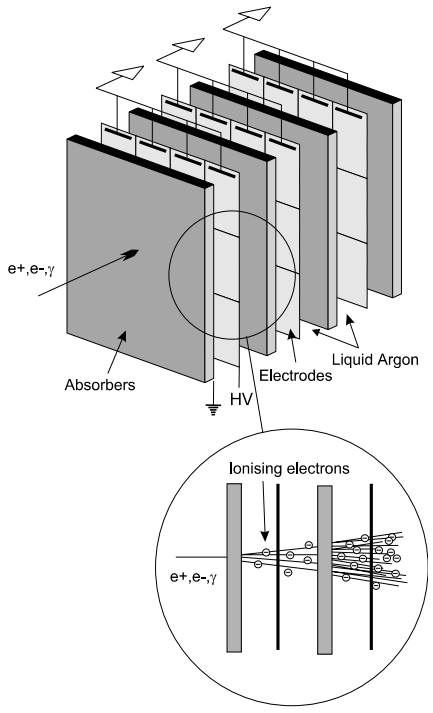

Figure 3-1: Principle of a sampling calorimeter

The number of electrons and positrons produced during this chain of events is proportional to the incident energy, and their presence is detected by the sensing system between the absorber plates, which are immersed in a bath of liquid argon. These liquid argon gaps are subjected to a large field strength. When one of the shower electrons or positrons produced in the absorber plates traverses the argon, it makes

a trail of electron–ion pairs along its path.

The electric field causes the ionization electrons to drift to the positive side (they move more quickly than the ions), and their motion produces an electric current in an external circuit connected to the calorimeter. The greater the incident energy, the more shower electrons are produced, and the greater the current. To determine the precise relation between this current and the corresponding electron or photon energy, one must calibrate the calorimeter. Figure 3-1 illustrates a LAr–sampling calorimeter and the development of an electromagnetic shower

3.2.2 Energy Resolution

The processes that govern the transformation of the incident particle energies into electrical pulses are statistical in nature. Thus, the response of the calorimeter will be different every time a particle of a fixed initial energy gets absorbed by it. The intrinsic resolution σ of a calorimeter is a measure of this relative spread in the distribution of measured particle energy. The fractional energy resolution is normally parametrized by the following equation:

$$\frac{\sigma}{E} = \frac{a}{\sqrt{E}} \oplus b \oplus \frac{c}{E} \qquad (3\text{-}1)$$

where $\oplus$ refers to adding in quadrature. The first term on the right–hand side of this equation is called the sampling term. As discussed above, the sampling takes place in the active medium between the absorbers. This is a statistical process where the measured energy is proportional to the number of charged shower particles N traversing the LAr–gap. The stochastic variable N is governed by Poisson statistics, thus the spread of N is proportional to $\sqrt{N}$. As N is proportional to the energy E of the incident particle, the relative resolution is given by $\sqrt{E}/E$ ($=1/\sqrt{E}$). This is the reason for the factor of $\sqrt{E}$ in the denominator. This term decreases in importance with increasing energy. The resolution can be improved by either increasing the frequency of sampling layers (i.e. more sampling layers per unit depth of calorimeter) or by increasing the thickness of each sampling layer.

The second term is referred to as the constant term, since it is independent of energy. This term can become dominant at high energies because the other two terms in the equation decrease with increasing energy. The constant term accounts for non–uniformities in calorimeter response caused by imperfections like mechanical non–uniformities and incomplete shower containment. In the case of hadronic calorimeters this term can also take into account differing response to electrons and pions (see Chapter 3.2.3).

The third term expresses electronic noise effects and normally becomes important at low energies.

3.2.3 Jets and Hadronic Showers

When a pair of quarks is produced and hadronizes, the states formed are low mass hadrons (mainly pions), all with a momentum in the approximate direction of the momentum of the initial quark or gluon. Therefore one say, that a ‘‘jet’’ of hadrons has been produced.

Neutral pions, from a jet incident on a calorimeter, or created in hadronic processes inside a calorimeter, will decay into two photons creating an electromagnetic shower, despite the fact that it is due to a hadron. The charged pions, on the other hand, will interact with nuclei, producing more and more particles until the energy of all of the particles is low enough that

all further losses take place via ionization (i.e. the energy becomes too low for nuclear interactions to take place).

3.3 ATLAS LAr Calorimeters

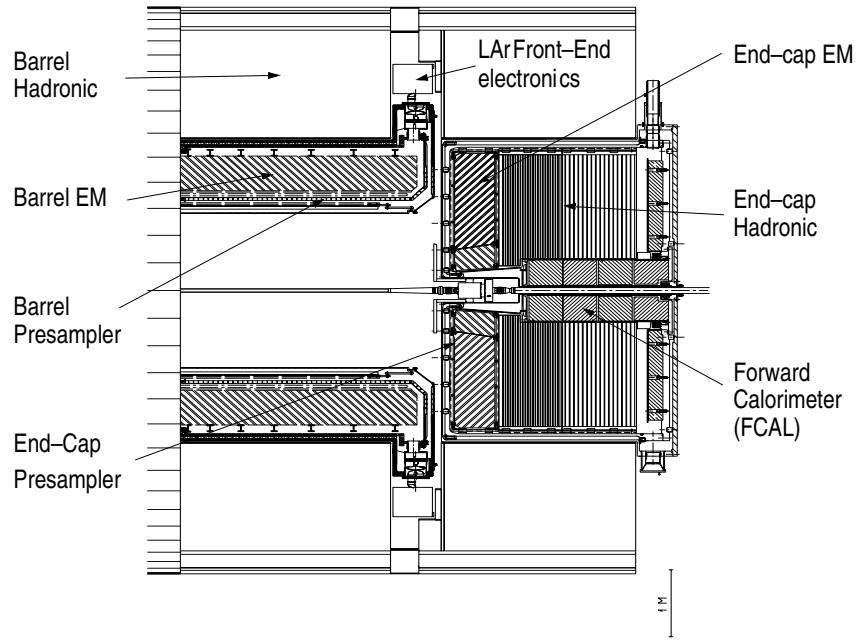

Figure 3-2: The ATLAS LAr–calorimeter system.

3.3.1 EM Calorimeters

Many of the important physics processes at the LHC involve decays to electrons or photons. Detection and reconstruction of these processes are very dependent on good electromagnetic (EM) calorimetry, which must fulfil strict requirements of acceptance, dynamic range, particle identification, energy resolution and direction measurement.

Physics Requirements

- The search for the Higgs boson sets limits on the energy resolution. An important channel for the Higgs boson search in the region 80–130 GeV is $H \rightarrow \gamma\gamma$. In this region the width of the Higgs is a few MeV [19]. The ability to resolve the invariant mass of the $\gamma\gamma$ pair will depend on how accurately the energy measurements can be done by the calorimeter. The requirements are a sampling term better than $10\%/\sqrt{E}$ and a constant term smaller than 1%.
- The calorimeter must also be able to reconstruct soft electrons in the range 1 to 5 GeV coming from semileptonic decays of b–quarks ($b \rightarrow c\, e\, \nu$). Reconstruction of these electrons will allow ATLAS to increase the b–tagging efficiency, which is important in the search for $H \rightarrow b\bar{b}$.

- Some extended gauge theories predict Z' and W' bosons with masses of 5–6 TeV. When these decay, energy of up to 3 TeV can be deposited in a single calorimeter cell, which sets the upper limit of the dynamic range in the electromagnetic calorimeter.
- Homogeneity is crucial in the search for processes involving missing P_T (i.e. supersymmetry).

An overview of the electromagnetic calorimetry in ATLAS is shown in Figure 3-2. It is divided into two major regions, barrel and end–cap, covering the pseudorapidity $|\eta| < 3.2$. Both the barrel and end–cap regions are sampling lead–LAr calorimeters with accordion geometries, shown in Figure 3-3a and b. In front of each of these calorimeters there are presamplers, designed to measure energy lost by early EM shower development.

The Barrel EM Calorimeter

The barrel electromagnetic calorimeter consists of two identical half–barrels covering the rapidity range $|\eta| < 1.4$. The active detector lies between 1500 mm and 1980 mm in radius and $|z| < 3150$ mm along the beam axis. There are 1024 accordion shaped absorber plates hermetically arranged around the beam axis in the ϕ direction. The structure of the accordion shaped absorbers was developed for LHC (see Figure 3-3). The advantage of this absorber shape is that the read–out electronics can be placed at the inner and outer radius of the electrodes instead of having it run along in a radial direction. This decreases the inductance of the signal connections to the on–detector electronics and thus, the time constant and the pulse shape for the read–out electronics can be improved. The accordion shape also allows for a full coverage in ϕ, without any gaps. Between two absorbers, there are two liquid argon gaps of 2×1.94 mm separated by a 300 µm thick read–out electrode. The electrode is made of multilayer copper clad kapton foil and is centred between two absorbers by light honeycomb spacers. Four of these double gaps are read out together to form a ϕ cell, this gives a segmentation of $2\pi/256 \approx 0.0256$ radians. In $|\eta|$, the segmentation is obtained by etching separate cells on the kapton read–out electrodes.

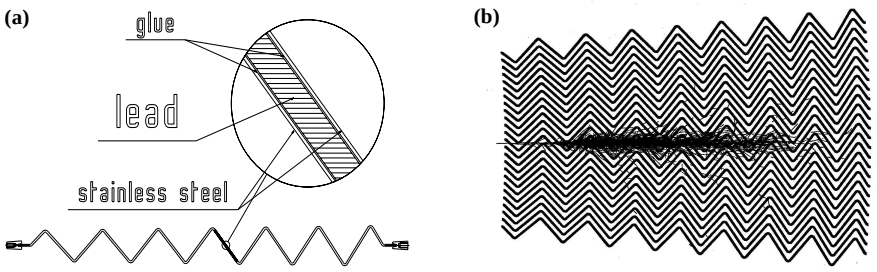

Figure 3-3: a) The accordion shaped absorber in the barrel EM calorimeter b) A simulation of an electromagnetic shower in the barrel EM calorimeter.

Simulations have shown that the minimum number of radiation lengths required for sufficient shower containment is $26.5\,X_0$. This means that the thickness of the lead in the absorbers must be 1.8 mm at η=0, but since the thickness of the calorimeter seen from the vertex increases with rapidity, the lead thickness can decrease with rapidity to improve the energy resolution. For technical and cost reasons, there is only one change in the lead thickness, which is 1.8 mm for $|\eta| < 0.9$ and 1.2 mm for $0.9 < |\eta| < 1.4$. To keep the liquid argon gap constant with depth, the first accordion fold at the calorimeter front end has a folding angle of 90.7 degrees, while the last fold at the back has a folding angle of 67.5 degrees. The ϕ

amplitude of the fold is approximately equal to the cell size in ϕ, i.e. $2\pi/256$ radians.

The End–Cap EM Calorimeter

Each end–cap calorimeter is mechanically divided into eight wedge–shaped modules. The accordion shaped absorber plates in this region, are arranged radially like the spokes of a wheel, with the folds running in the radial direction. Furthermore, to ensure good uniformity everywhere, the combined thickness of liquid argon and absorber crossed by the particles must be independent of the azimuthal angle. This leads to a folding angle for the absorber which varies with the radius. The liquid argon gap also increases with radius. Since the lead thickness is constant, the drift field is adjusted to vary with radius to obtain a uniform signal response. The total thickness of the calorimeter is greater than $28\,X_0$ for all rapidity values.

Presamplers

A particle moving outwards from the vertex of the p–p collision will, before entering the electromagnetic calorimeter, have to traverse a lot of "dead" material consisting of the Inner Detector, the solenoid and the cryostat. This may cause the particle to develop an electromagnetic shower outside the calorimeter. To measure this a thin active layer, called the presampler, will be placed in front of the calorimeter inside the cryostat. It gives information of how far the shower has developed. Liquid argon will also here be used as active medium and printed circuit board strips, approximately 1 cm high and 300 µm thick, will be placed pointing to the vertex with a slight tilt with respect to the trajectory of the incoming particle. The presampler segmetation in the η direction is the same as for the middle layer of the barrel calorimeter and in ϕ one cell corresponds to 4 cells in the calorimeter. The endcap presampler follows the same principle but has a thinner active region than the barrel (6 mm).

3.3.2 Hadronic Calorimetry

The main tasks in hadronic calorimetry in ATLAS are:

- To identify jets and measure their energy for inclusive cross–section measurement (jet spectroscopy).
- To measure missing transverse energy, an important signature in many physics processes.

This is accomplished with the help of the electromagnetic calorimeters.

The End–Cap Hadronic Calorimeter

Due to the extreme radiation levels expected in the forward region of ATLAS a scintillating tile calorimeter as in the barrel region is not feasible. The hadronic end–cap calorimeter is therefore a sampling copper–liquid argon calorimeter. Its position in the ATLAS calorimeter system is illustrated in Figure 3-2. The end–cap has two major divisions in *z*, referred to as wheels. The first wheel contains 24 read–out cells, while the second wheel contains 32 read–out cells. The spatial resolution requirement is fulfilled by having a segmentation of $\delta\phi \times \delta\eta \cong 0.1 \times 0.05$ for $|\eta| < 1.9$ and 0.1×0.1 for $|\eta| > 1.9$. The hadronic end–cap will be about $10\lambda^{\dagger}$ deep, and will extend over a pseudorapidity range from $1.5 \le |\eta| \le 3.2$. Since it is at such high η, the hadronic end–cap must operate in very high radiation conditions. Copper was chosen over the standard iron or steel absorber because of it's shorter interaction length.

† The interaction length λ is defined as: $\lambda = 1/(n \cdot \sigma_{abs})$ where *n* is the atomic density of the material and σ_{abs} is the total absorption cross–section.

The Forward Calorimeter (FCAL)

In order to have as full coverage for jets in ATLAS as possible, a forward calorimeter covering $3.1 < |\eta| < 4.9$ is required. It will be an essential part of forward jet–tagging in the search for a heavy Higgs boson which decays to jets via W or Z bosons. Due to the extreme particle flux and high radiation levels a specially designed forward calorimeter is being constructed. It is a liquid argon calorimeter composed of three modules. The first module is an EM calorimeter made with copper or brass absorbers. The second and third modules are hadronic and its absorbers are made of a combination of stainless steel and a tungsten alloy. A structure based on rods and tubes has been chosen for the FCAL. The LAr gap width is maintained constant by wrapping a quartz fibre around the tube and allowing liquid argon to fill the narrow (250 µm) gap between the rod and the tube.

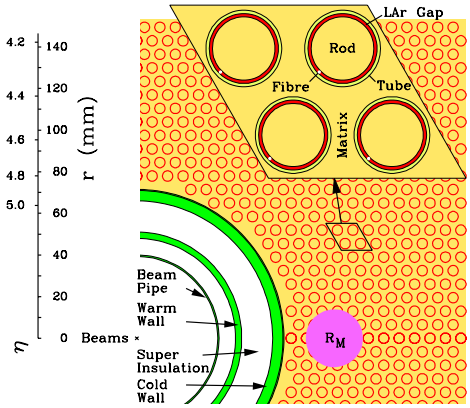

Figure 3-4: The front face of an EM FCAL module. R_M indicates the "Molière radius". The shower is roughly contained in a cylinder with the radius $2R_M$.

3.4 LAr Electronics

All LAr calorimeters deliver on their electrodes a triangular–shaped current pulse (see Figure 3-5) with a fast rise time of a few ns. The pulse decreases to zero at the end of the drift time of the ionization electrons in the liquid argon. This takes about 450 ns (except for the FCAL ~50 ns, since the argon gap is smaller). The amplitude of the current varies from one sub–detector to another. This signal is delivered on the detector impedance which, to a very good approximation, is a pure capacitance from as low as 20 pF to as high as 3 nF.

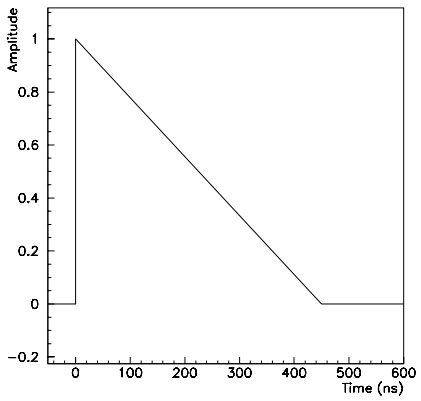

Figure 3-5: Signal shape as produced in the detector (triangle),

3.4.1 Requirements

The main requirements for the LAr read–out electronics can be summarized in the following points:

- The dynamic range to be covered must be at least 16 bits. This demand is linked to the fact that the energy in a single read–out cell can be as large as ~3 TeV (see 3.3.1) and on the low end, energy deposits arising from multiple interactions in a single crossing pro-

duces an energy distribution whose mean and width is ~50 MeV. This distribution can be described statistically and is given the name “pile–up noise”.
- The LAr calorimeters measure energy with a relative resolution of ~10%/√E, reaching a lower limit at high energy set by various imperfections of ~0.5%. The read–out electronics should not degrade this performance except for unavoidable electronics noise which contributes significantly only at low energy. In particular, to maintain a small constant term in the energy resolution, the read–out system should be calibrated to better than 0.25% over the whole energy range.
- The amount of coherent noise per cell should be less than 5% of the level of incoherent noise. The reason for this is that, when measuring the energy of an electromagnetic shower or of a jet, one add up the energy measured over many cells (~100 to ~1000).
- The read–out system must sample the signals at 40 MHz without introducing any additional dead time. To achive this a pipeline with a depth of at least 2.5 µs is provided, which combined with a large enough derandomizing buffer and a fast enough read–out, will allow for a LVL1 trigger rate up to 100 kHz.
- The large number of channels (~190 000) requires a system with low power consumption and low cost.
- Since the electronics will be located in an area with limited access, high reliability is of great concern.
- Finally, the electronics has to be radiation tolerant. Since this is the topic of this thesis, the reader is referred to the following chapters for a closer discussion.

3.4.2 The Front End System

The raw calorimeter signal is processed by the so–called front–end system, which is the part of the electronics system that provides for preamlification, shaping, digitising. The whole system is mounted on a single, 10–layer double–sided, printed circuit board, called front–end board (FEB). The FEBs are grouped into crates mounted on the flanges of the liquid argon calorimeter, (see Figure 3-2). The front–end system has to read out all the sub–detectors discussed in this chapter (EM calorimeters+presamplers, hadronic end–cap and forward calorimeters) with ~190 000 channels in total. Figure 3-6 shows schematically the front–end system with the different boards and links to the rest of the electronics. Their function is described briefly below.

Preamplifiers

Preamplifiers are used to amplify the detector signal to be above the noise level of downstream electronics and should therefore be the only contributor to the electronics noise. This is done in the most efficient way if the preamplifiers are located as close to the detector as possible, preferably inside the LAr cryostat. However, the high radiation levels in the EM calorimeters led to the development of preamplifiers coupled to the detector through transmission lines. This allows for the preamplifiers to be located remotely, in the front–end crate, where there is a reduced radiation field. To minimize any coherent noise pick–up at the preamplifier input, these circuits are enclosed in a Faraday cage. All EM calorimeters are read out using this scheme. High speed silicon bipolar transistors, that will provide adequate radiation hardness, are used in these preamplifiers.

Shaping Amplifiers

Shapers are the input to the sampling stage, and one of their functions is to limit the system bandwidth to match the 40 MHz sampling frequency. In addition, to minimize the baseline shift, a bipolar CR–RC^2 prefilter is adopted. The shaping time constant (chosen to minimise

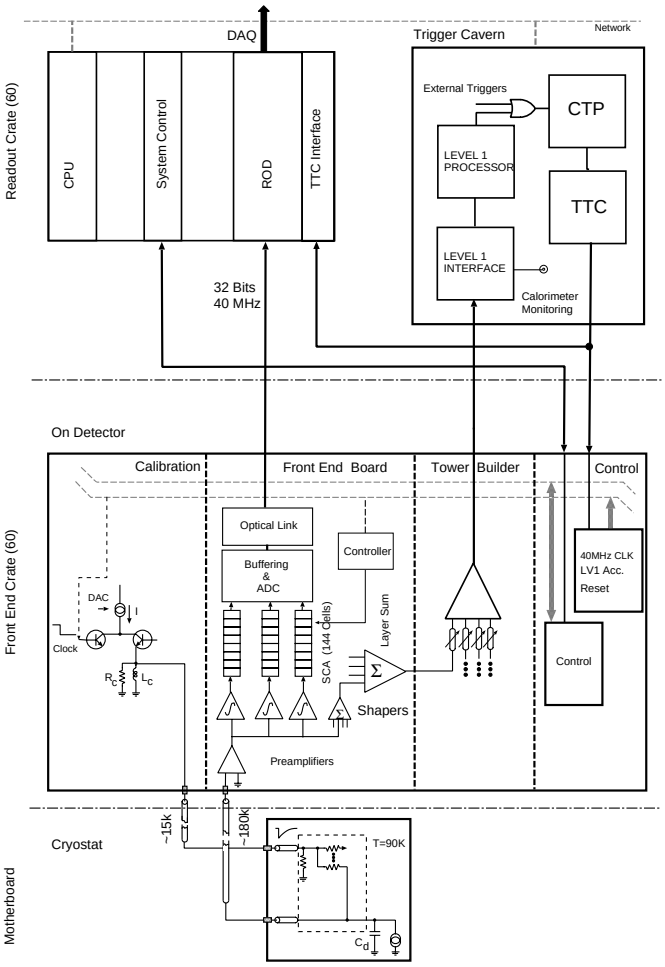

Figure 3-6: The LAr electronic system.

the combination of electronic and pile–up noise) is not critical, as downstream digital processing can modify it, which is an advantage since the optimum shaping time is luminosity–dependent. Figure 3-7 illustrates the pulse shape after this stage.

Since it is not possible to handle the 16–bit dynamic range of the input signal on a single gain scale, without degrading it, multiple ranges are used to extend the dynamic range. A system with three ranges has been chosen. Thus for each input, the shaper produces three output signals with gains in the ratio 1/10/100. Each gain has a dynamic range better than 12 bits.

Analog Pipeline and ADC

The signal from the shaper output is sampled at 40 MHz. The phase of the sampling clock is adjusted so that one sample is taken ±2 ns from peak of the shaped pulse. The results is stored in an analog pipeline memory during thee first–level trigger decision (2.5 µs maxi-

mum). The pipeline is 144 cells deep, enough memory to store seven events with five samples each in addition to the 100 cells used to cover the LVL1 trigger latency.

Upon receipt of a LVL1 trigger accept signal typically five samples around the peak of the pulse belonging to the triggered bunch–crossing are digitized by a 12–bit ADC. One ADC digitizes the signals from eight calorimeter cells. The same gain is used for all samples in order to minimize systematic effects due to small differences in pulse shapes of the different gains.

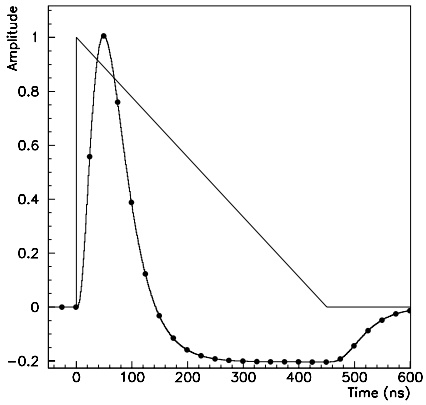

Figure 3-7: Signal shape as produced in the detector (triangle), and after shaping (curve with dots). The dots represents the different samplings.

Optical Link

Last in the line of components in the front–end system, is the optical link, which the work described in this thesis centres on. The link will transfer the data from the FEBs to the so–called read out drivers (ROD) that are located ~100 m away from the detector.

It's required that 32–bit words are transmitted over the link at a rate of 40 MHz. If a single fibre is used, the link therefore has to be able to send data at a rate of 1.28 Gb/s.

As there are ~190 000 LAr calorimeter+presampler channels in total, and each link transfers data from 128 channels (assuming there is one data link per FEB), a total of ~1500 links are needed. The event rate can be calculated as follows:

- One FEB delivers data from 16 ADCs
- One ADC produces 16–bit words (12 data–bits and 4 bits with information about gain and parity) by digitizing signals from 8 calorimeter channels. A minimum of 5 samples around the peak are taken.
- In addition 10 16–bit words are added with information about bunch–crossing, ADC number, FEB number etc.

This gives in total 800 16–bit words or, 400 32–bit words, that must be transmitted for every event. Given the speed of the link (1.28 Gb/s) this takes 10 µs. Thus, the link has the capacity to transfer events at a maximum rate of 100 kHz, corresponding to the maximum LVL1 trigger rate. The format of the LAr data words has been established and is illustrated in Figure 3-8.

3.4.3 The Read Out Drivers

The LAr off–detector electronics is located in so–called Read Out Crates (ROC). Typically there will be one ROC for each front–end crate. Each ROC will contain many Read Out Driver (ROD) modules. Each ROD is connected to two FEBs. The RODs are the last detector specific stage in the ATLAS. They are responsible for processing the data from the FEBs, and subsequently making the processed data available to the Data AQuisition (DAQ). The ROD output data will consist of the reconstructed energy, time, and data quality.

In addition to the RODs, each ROC contains a TTC (Timing, Trigger, and Control) interface

which receives information (trigger number, bunch–crossing number, etc.) from the LVL1 trigger required in the data transmitted from the FEBs.

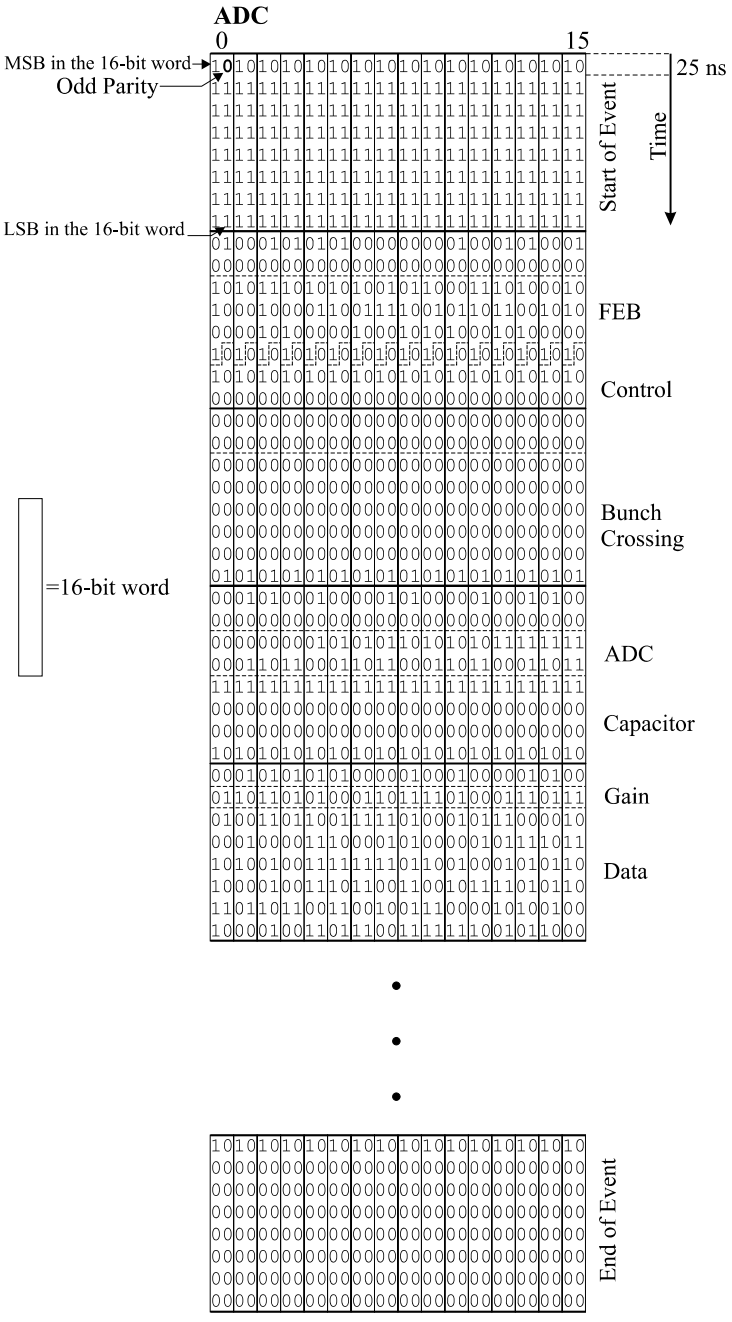

Figure 3-8: The structure of the 32–bit data words that will be transmitted over the LAr optical link. One of these events contains information about energy and gain from 128 calorimeter cells (one FEB).

CHAPTER 4

THE OPTICAL LINK

A radiation tolerant optical link is used to transfer data from the front–end boards to remote read–out drivers located up to 200 m away. The LAr optical link will be composed of a serialiser, an optical transmitter (a Vertical Cavity Surface Emitting Laser diode, VCSEL, and supporting electronics in this case), an optical channel (a fibre), and an optical receiver (a PIN–diode and supporting electronics) with associated optical and electrical connectors. In this chapter a demonstrator link composed of these components is described.

4.1 Why Optical links

At present particle physics experiments, data is primarily being transferred off–detector by copper cables. As discussed in the previous chapter, the sub–detectors in ATLAS must be highly granular to be able to resolve the vast number of particles created in the p–p collisions. The large number of links, needed to transfer data from all channels, makes the use of copper cables undesirable due to their large volume and density which would interfere with particle detection. It is also expected that copper cables would lead to problems with ground loops generated by the shielded cables connected to the detector. Non–metallic optical links allow detector subsystems to be decoupled from off–detector electronics, reducing coherent noise problems from ground loops. On–detector multiplexing significantly reduces the number of links needed to transfer information off the detector. For the distances and the data rates under consideration optical links attenuate and distort signals much less than copper links. For a given data–transfer rate, optoelectronic components are usually smaller and require less power than their copper counterparts. Finally, cost is always an important factor and the prices for optoelectronics components and fibres continue to fall as they become established on the market. Table 4-1 summarises the number of data channels and links used by the different sub–detectors to transfer data from the front–end eletronics to the read–out drivers [20].

Sub–detector	**No of data channels**	**No of links**
Pixel	140 000 000	4 500[a]
SCT	6 000 000	8 000[a]
TRT[b]	420 000	27 000
LAr calorimeters+presamplers	200 000	1 600
Tile calorimeter	10 000	250[c]
Muon system	1 300 000	2 700[c]

Table 4-1: A summary of the number of data channels and optical links in ATLAS.

a. Bidirectional
b. The TRT uses exclusively copper links.
c. These numbers can change.

4.2 Link Requirements

The LAr calorimeter links must satisfy strict requirements on the amount of data that must be transferred, the relatively high radiation levels prevailing at the location of the front–end electronic crates and the limited access to the same. Some of these requirements are listed

in Table 4-2 [20].

In Chapter 3.4.2 the LAr optical link was briefly discussed. The link transmitter is located on the LAr FEBs (front –end boards). Although the space between cooling plates mounted on either side of the FEB is restrictive, optoelectronic components packaged in a standard commercial forms can be used along with conventional fibre optic connectors. The links are unidirectional as control data is sent to the electronics crate over dedicated links (outside the scope of this work) and then distributed to the various electronic cards. The links must be able to transfer data over a distance up to 200 m, at nominal rate of 1.28 Gb/s (32 bits @ 40 MHz). However, coding protocols require additional control bits and the overall requirement for the transfer rate could be as high as 1.6 Gb/s. The magnetic environment in which the links must operate is on average 0.4 T. Finally the presence of radiation fields means that all candidate components need to be thoroughly tested.

Number of Links		1620
Length [m]		100–200[a]
Data Format		32 bits
Clock Speed [MHz]		40
Data Rate [Gb/s]		1.28
Ionising dose [Gy]	Tx	800
(10 yrs LHC running)	Rx	0
Neutron fluence [n/cm^2][b]	Tx	1.7×10^{13}
(10 yrs LHC running)	Rx	0
Max. Power Dissipation [mW]		3000

Table 4-2: Specifications for the LAr optical link [20]

a. This depends on the location of the RODs, underground or at the surface.
b. 1MeV(Si).

As the length of the link, is short (less than 200 m), the product of data rate and distance is moderate. A solution based on commercial components is therefore feasible. However, the transmitting side of such link must be tested and proven to withstand the radiation doses mentioned above.

4.3 The Demonstrator Link

The final LAr link architecture has not yet been decided upon but a demonstrator link with the following structure has been developed:

serialiser $\Rightarrow$ laser driver+emitter $\Rightarrow$ fibre $\Rightarrow$ PIN–diode+receiver $\Rightarrow$ deserialiser

This arrangement is shown schematically in Figure 4-1. The serialiser and deserialiser comes from Aglient Technologies® and is commonly referred to as the G–link. The transmission and reception sides are connected together with 50/125 GRaded INdex (GRIN) multimode optical fibre through industry standard SC–type connectors. The laser emitter is a Vertical Cavity Surface Emitting Laser (VCSEL) and the optical receiver is a PIN–diode. These two are used as the trasmitting and receiving part of a dual port transceiver module. A Programmable Logic Array (ALTERA® EMP7128) is placed on the receiver board to interface error status information from the deserialiser to the data acquisition system.

The demonstrator link has been tested successfully in the laboratory and no errors were seen

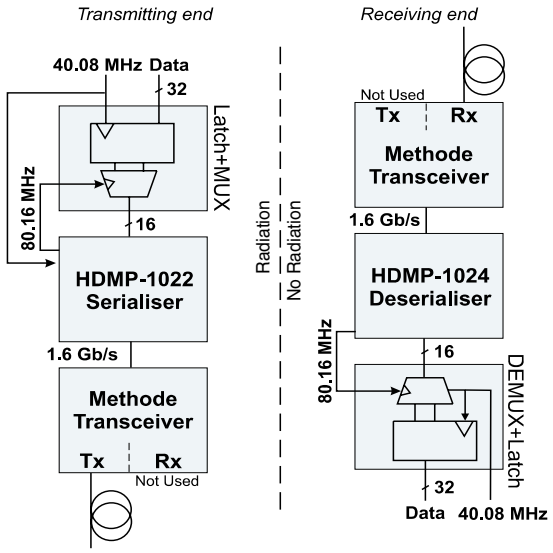

Figure 4-1: A Gb/s demonstrator link based on the G–link chipset. In the figure a scheme for multiplexing the 32 bit data to fit the 16 bit structure of the G–link is also shown. However, this has never been implemented in any of the tests described in the following chapters. Without this multiplexing every 16 bit data word is sent twice, given a frequency of 40 MHz. In the final link solution a multiplexer will be built in a radiation hard DMILL technology [21].

during several months of operation. Each of the component parts of the link are described in more detail in the following section.

4.4 Key components

4.4.1 VCSELs

When choosing the optical source for the link, interesting features are cost, speed and radiation tolerance. Light emitting diodes (LEDs) are very cheap, but they are also relatively slow. The only alternative to LEDs are laser diodes. The least expensive lasers are those produced for CD– and DVD–players at operating wavelengths of 780 nm and 655 nm, respectively. However, they are edge–emitting sources, which would result in a large pulse spreading due to material dispersion and are not packaged for use with optical fibres. Conventional edge–emitting telecommunications lasers operating at 1300 and 1550 nm are presently rather expensive. VCSELs (Vertical Cavity Surface Emitting Lasers) on the other hand, are commercialized as a light source for short haul high speed multimode fibre applications [22]. The VCSEL laser diode is a strong candidate for use at the emitting end of the LAr data link. VCSELs have a number of desirable properties such as:

- Low cost of manufacture as the devices can be tested on the wafer prior to dicing.
- Circularly symmetric optical output which makes it easy to couple efficiently to multimode fibres.
- The surface emitting structure and small mode size enables production of highly uniform and densely packed lasers, with minimal crosstalk, for use in parallel optical links.
- High output power for a modest bias current (1 mW at 10 mA bias, typically).

- Low threshold currents (typically, a few mA).
- The VCSEL has a small active volume. This provides a smaller damage cross section in a radiation environment [23].

Laser diodes produce light primarily by stimulated emission whereby a photon stimulates an excited electron to recombine with a hole and produce another photon with the same frequency, direction of propagation, and phase.

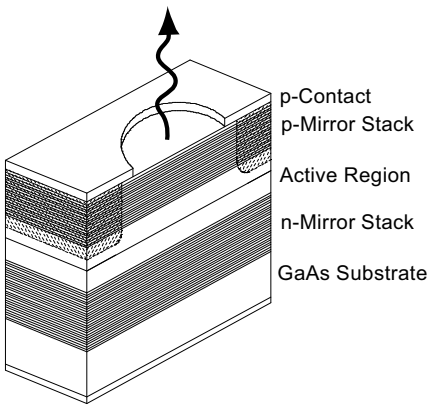

Figure 4-2: Schematic of a VCSEL.

VCSELs are essentially LEDs constructed in the form of a Fabry–Perot cavity. The VCSELs used in this work are designed to emit light at 850nm. The structure of a typical VCSEL is shown schematically in Figure 4-2. The p–mirror stack consists of a number of alternating layers of AlAs/Al–Ga–As. The active region contains three GaAs quantum wells surrounded by Al –Ga–As spacers. The n–mirror consists of a number of AlAs/Al–Ga–As pairs grown on an n–type GaAs substrate.

Work done by Honeywell [22] shows a typical forward voltage and light output versus current relationship for temperatures of 10, 40 and 70°C according to Figure 4-3. The laser threshold current is seen to be stable within 1mA over approximately 80°C temperature variation. This allows VCSELs to be used in an open loop driving circuit, significantly reducing the cost. The forward operating voltage is typically 1.8V with a series resistance of 20Ohms. Typical slope efficiencies are 0.2mW/mA.

In the tests described in the next chapter, all the VCSELs are encapsulated in TO–46 packages (see Figure 4-5). These can pe equipped with either a flat window or a lens for better coupling to an optical fibre. Packaging is actually the most dominating factor in when it comes to the price of the VCSEL.

4.4.2 Optical Fibres

An optical fibre is a waveguide for electromagnetic waves with wavelengths in the µm region. Not all wavelengths can propagate in a fibre, but only those that are solutions to Maxwell's equations with the particular boundary conditions set by the shape and dimension of the fibre. These particular solutions are referred to as "modes". A "multi–mode" fibre can

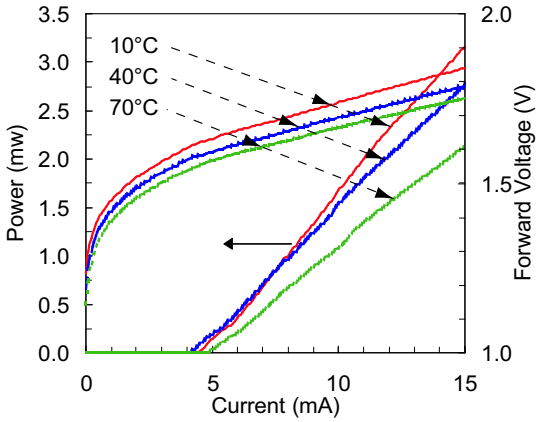

Figure 4-3: Characteristics of a typical VCSEL.

transfer multiple modes as opposed to a “single–mode” fibre which can only sustain a single mode.

When a pulse of light propagates down a fibre, it’s width increases. This pulse spreading results in a limit on the modulation frequency that can be transmitted by the fibre. Pulse spreading is mainly due to three factors:

- material dispersion,
- waveguide dispersion,
- multimode distortion.

Waveguide dispersion is negligible compared to material dispersion as long as the optical wavelength is less than ~1 µm. Waveguide dispersion and material dispersion add algebraically, and by altering the profile and magnitude of the material index of a fibre, the zero dispersion wavelength can be shifted to 1.55 µm (where the optical absorption is at minimum). This attenuates the dispersion curve over a region of wavelengths [24].

Modal distortion occurs in a multi–mode optical fibre were pulses experience spreading due to the fact that each fibre mode has a different refractive index and therefore a different group velocity. To minimize pulse spreading a single mode fibre should therefore be chosen. However, to maintain a single mode, the core of the fibre is small (about 9 µm). As a result, the optical coupling efficiency is small and connections and splices must have excellent alignment. Multimode fibres, because of their large core diameter (50 to 100 µm), have a very high optical coupling efficiency and connections in multimode fibre are less sensitive to misalignment.

A decrease in modal distortion can be achieved by grading the index profiles of multi–mode fibres. The idea of a GRIN fibre is to make the optical paths, travelled by the various modes, equal, as shown in Figure 4-4. The lowest order mode corresponds to light that travels parallel to the central axis of the fibre where the index is highest. A higher order mode corresponds to light that makes many bounces when it travels down the fibre, and thus spends significant time near the core–cladding boundary. By making the index lower near the core–cladding and increasing to a maximum at the centre of the core, the total travel time of rays corresponding to high order and low order modes can be made nearly equal, reducing the total modal distortion. For applications where the fibre length is up to a few hundred meters,

data rates in excess of a Gb/s can easily be achieved.

For the ATLAS LAr optical–link, it is proposed to use a multimode GRIN fibre with a nominal core diameter of 50 µm†.

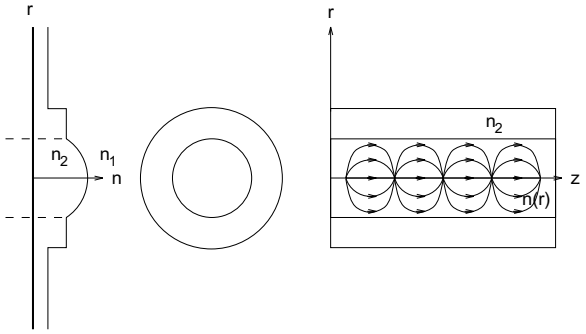

Figure 4-4: Graded index fibre (GRIN) , (left) profile of the refraction index as function of radius.(middle) fibre cross section (right) light ray paths in the fibre [25].

4.4.3 Transceivers

Transceivers are dual port modules, which can transmit data via one port and receive data through the other. The transmitter part consists of a driver circuit coupled to a VCSEL. The optical receivers [26] in most commercial VCSEL transceivers consists of PIN photodiodes with associated circuitry (discriminator and a preamplifier). Both the transmitter and receiver can be coupled to an optical fibre with an industry standard SC connector. Transceivers are unlikely to be a part of the final link solution. They are however used in the demonstrator link as a cheap and simple solution.

4.4.4 PIN–diodes

PIN–diode‡ is a light sensitive device whose operational principle can be described as an LED working “backwards”. Instead of a radiative *recombination* of electron–hole pairs as in the LED, a photon induced *creation* of electron–hole pairs take place, contributing to the generation current. As the diode is operated with reverse bias, this extra generation current will give rise to a signal in an external circuit.

As the PIN–diode will be located in the receiving end of the link, it is not required to be radiation hard. Because of the VCSEL operating wavelengths near 850 nm, either Si or GaAs are commonly used for the PIN detector. As GaAs PIN–diodes are inherently fast, they are used in some low cost VCSEL transceivers, although silicon is cheaper.

4.4.5 The G–link Serialiser

Since 32 bit words are to be sent over a single fibre the data has to be serialised. The only commercial serialiser available at the time this work started, that could send meet the re-

† Optical fibres are classified according to: ‘core–diameter’/’diameter of primary cladding’. e.g. 50/125.

‡ The letters P I N indicates the doping profile: p–type, intrinsic, n–type.

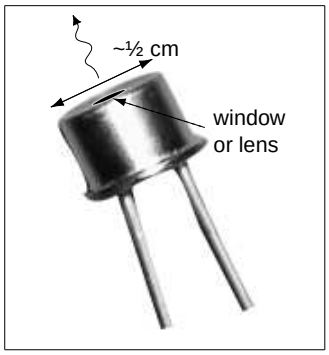

Figure 4-5: (left) A VCSEL in a TO–46 package.

Figure 4-6: (right) A transceiver module with two SC–connectors.

quirement of 1.6Gb/s transfer rate, is called G–link [27] and is manufactured by Aglient Technologies®†. It consists of one transmitter chip (HDMP–1022) and a receiver chip (HDMP–1024). From the user viewpoint it can be thought of as a "virtual ribbon cable" for transmission of parallel data. Data in the form of 16 bit words‡ loaded into the transmitter (Tx) chip is delivered to the receiver (Rx) chip over a serial channel, which can be either a coaxial copper cable or optical link, and is reconstructed into its original parallel form.

As a result of the G–link protocol (CIMT, Conditional Invert Master Transition) an additional 4 bit control word is added to every 16 bit data word, making a 20 bit frame. The control field denotes the data type being sent, and contains the encoded clock in the form of a "master transition bit" which the Rx chip uses for frequency locking. When data is not available to send, the link maintains synchronization by transmitting fill frames. Figure 4-7 shows the principle of the master transition and the structure of the fill frames. To inhibit

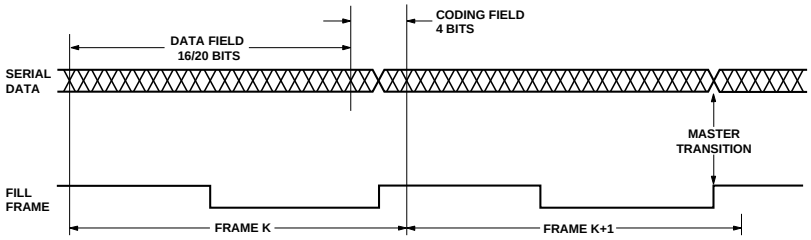

Figure 4-7: The structure of the serial data and the fill frames for the G–link. The "master transition" is used by the Rx for frequency locking.

collection of charge at the receiver the serial line DC balance is maintained automatically by keeping track of the cumulative sign of the outgoing data and, whenever its necessary,

† Formerly Hewlett Packard.

‡ Since the LAr data is 32 bits wide a multiplexing must be performed to fit the G–links 16 bit word width.

inverting a word to shift the duty cycle closer to the desired value of 50%.

To fulfil our requirements of speed the G–link has to run in “double frame mode”. When used in this mode, an internal clock signal with double the frequency is generated by the G–link Tx and the data can be clocked in twice as fast, giving the desired total link throughput of 1.6Gb/s.

The G–Link can perform basic error checking by monitoring the control field for illegal conditions. An “ERROR flag” indicates an illegal control field in the transmitted frame. A “LINKREADY flag” occurs when the G–link receiver cannot identify a frame to lock onto. Note that the assertion of the ERROR flag *does not* implicate that there is something wrong in the data field.

The chipset is manufactured in a monolithic silicon bipolar “sea of gates” technology with 25GHz transistors. The transmitter has PECL compatible serial outputs which allows it to drive transceivers directly. The inputs are standard TTL. The power dissipation is 1.9 and 2.5W for the Tx and Rx chip respectively. The transmitter and receiver chip are packaged in an aluminium M–Quad 80 package to promote heat dissipation.

–♦–

CHAPTER 5

RADIATION ISSUES

The basic mechanisms of radiation effects on electronics are reviewed in this chapter. Topics discussed include the effects of displacement damage and ionizing radiation, single–event phenomena and radiation effects on VCSELs, fibres and Integrated circuits. A method for evaluating the rate at which neutron induced single–event upsets (SEU) occur in ATLAS, given the neutron energy spectrum present at the LAr electronic crates, is also presented.

5.1 Radiation Environment in ATLAS

The three major sources of radiation at the LHC are:

- particle production at the interaction point
- local beam losses
- beam–gas interactions

The total beam loss in the accelerator will not exceed 10^7protons/s. Beam–gas interactions are estimated to be ~$10^2 s^{-1}$ in the interaction area. These losses are small compared to the p–p collision rate of ~10^9protons/s at each interaction point. Thus, the major part of the radiation will come from particles produced in the proton collisions at the interaction point. The enormous rate of these collisions causes direct radiation damage to detectors, electronics and optoelectronics. An additional effect is activation of detector parts, which leads to radiation backgrounds in the detector.

For the Inner Detector, the primary radiation consists of the particles created in the p–p collision and their decay products, which predominantly includes the lowest mass hadron states; protons, pions and kaons. Most of these will be absorbed in the calorimeters. As mentioned in Chapter 3, when high energy hadrons hit the calorimeter a hadronic shower is formed due to nuclear interaction with the calorimeter absorber material. The content of this shower is protons, neutrons and short–lived particles which eventually will decay to protons and neutrons. The protons will loose their energy to ionisation, but the neutrons will either be captured by a nucleus or loose their energy in non destructive collisions with the absorber atoms and become thermalised. Associated with these nuclear interaction processes is the production of gamma–photons.

Flux, Fluence & Dose

The rate of particles incident on a material is given in terms of the particle flux, expressed in particles·$cm^2 \cdot s^{-1}$. The time integral of the flux is referred to as the particle fluence, expressed in particles/cm^2.

Radiation induced damage depends on incident particle energy as well as on which material is being exposed. For neutrons, the normal procedure is to use, so called, "kerma–factors" to normalise the flux so that it is equivalent to 1 MeV neutrons incident on a specific material. The notation for this in the case of silicon is: n(1 MeV(Si)) ·$cm^2 \cdot s^{-1}$

The energy deposited in materials by ionizing radiation is expressed in terms of the “absorbed dose”. The SI unit of absorbed dose is the Gray (Gy), which is equal to an absorbed energy of 1 Joule per kg. The energy loss per unit mass differs from one material to another because of differing atomic properties. Therefore one usually indicates this (e.g. Gy(Si) for silicon). Ionizing dose rate is commonly expressed in Gy/s.

The particle production discussed above contribute to the radiation damage the detectors and their associated electronics. Activation of the same also occurs due to both spallation products from energetic hadrons and neutron capture. Detailed estimates of the ATLAS radiation environment can be found in [13] and references therein.

5.1.1 Simulations

The following estimation of the ATLAS radiation environment is based on simulations carried out by others [13] with the DTUJET [28] code for generating p–p minimum–bias† interactions, and with the FLUKA [29] code for transporting and showering the secondary particles created by DTUJET. Simulations have also been carried out using DTUJET together with GCALOR [30] (a program package that can simulate neutron interactions down to thermal energies). Whenever consistent geometrical and material descriptions have been used, the results of the two codes agree with each other to within 30% or better [13].

The work described in this thesis concerns neutron and photon radiation exclusively. There are also proton and electron radiation present at the position of the LAr electronic boxes. However, the levels of these are orders of magnitude lower, due to the shielding from the calorimeters‡, and are not believed to cause any significant effects. Less emphasis has therefore been put on simulations of these radiation types.

The simulated neutron spectrum at the position of the LAr front–end electronics, resulting from these simulations, is shown in Figure 5-1. This spectrum is extremely peaked towards lower energies (95% of the neutrons have energies below 1MeV). This is a result of the

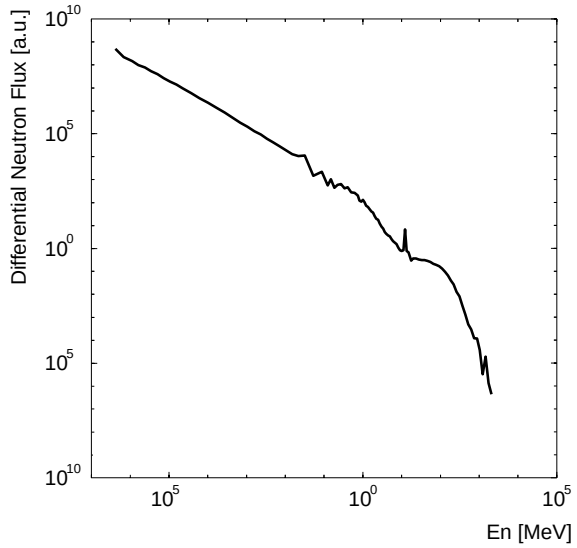

Figure 5-1: The ATLAS neutron spectrum. The bump at 10MeV is an unexplained artifact from the simulations.

thermalisation the neutrons undergo in the calorimeters. In Figure 5-*i* and Figure 5-*ii* on the next page flux and dose maps throughout the ATLAS detector system, for neutron and gamma radiation, are illustrated. The position of the crates, where the LAr front–end electronics and the transmitting end of the optical link is located, has been indicated in the figures.

† "Minimum bias" events are soft p–p interactions with small p_T that will dominate the ~23 interactions in every bunch crossing.

‡ Since protons and electrons are charged they are, to a large extent, absorbed in the calorimeter. After all, this is the idea of such device.

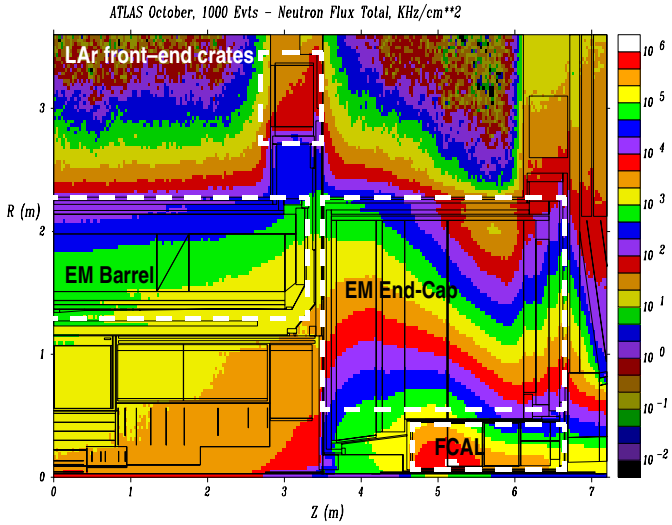

Figure 5-i: The neutron flux in the calorimeter and its vincinity.

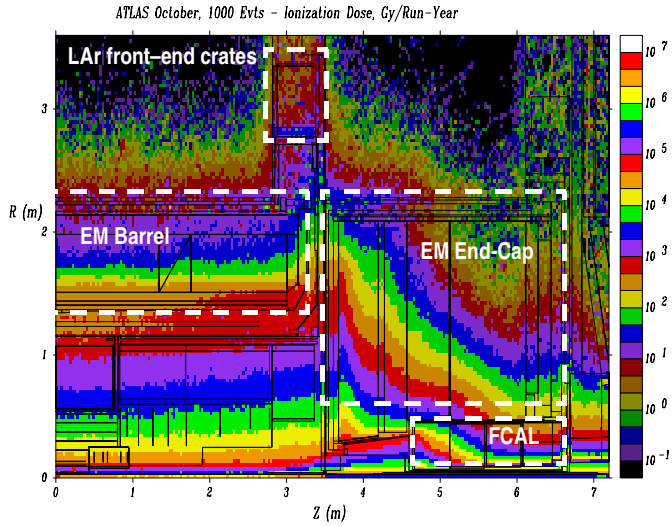

Figure 5-ii: The photon ionising dose in the LAr calorimeter and its vincinity.

Table 5-1 shows the ionisation doses, dose rates, fluxes and fluences after 10 years of LHC operation for the EM calorimeter. To account for simulation uncertainties a safety factor of 3 has been applied to get this values.

Ionising dose	800 Gy(Si)
Ionising dose rate	30 Gy(Si)/h
Neutron fluence	1.7×10^{13} n(1MeV(Si)) cm^{-2}
Neutron flux	6×10^{8} n(1MeV(Si)) cm^{-2} h^{-1}

Table 5-1: Ionisation doses, dose rates, fluxes and fluences after 10 years of LHC operation for the ATLAS EM calorimeters.

5.2 Particle Interactions

As radiation damage to semiconductor materials (described in the next section) is usually classified as “ionising” or “non–ionising”, this section is structured accordingly. Charged particles can undergo both ionising and non–ionising interactions. Photons normally cause ionisation. Neutrons never give rise to direct ionisation since they are neutral and always interact directly with the atomic nucleus. However, interactions by secondary charged particles created in these nuclear interactions are often ionising.

5.2.1 Ionising Interactions

Photons

Photons have zero rest mass and are electrically neutral. They interact with atoms mainly through three processes; photoelectric effect, Compton scattering, and pair production. In all three cases, the interaction produces energetic free electrons.

The probability of a photoelectric interaction decreases with increasing photon energy and increases with the atomic number Z of the material. If the incident photon is energetic enough to emit an electron from the K shell, then collisions with K–shell electrons are the most probable. In the photoelectric process, the incident photon energy is completely absorbed by the emitted electron (photoelectron) that appears with an energy given by $E_{e^-} = h\nu - E_b$, where E_b represents the binding energy of the electron in its original shell. If this happens to be the K–shell, an electron from the L–shell will drop into the empty state, which will cause a characteristic X–ray or a low–energy Auger electron to be emitted, depending on the value of Z.

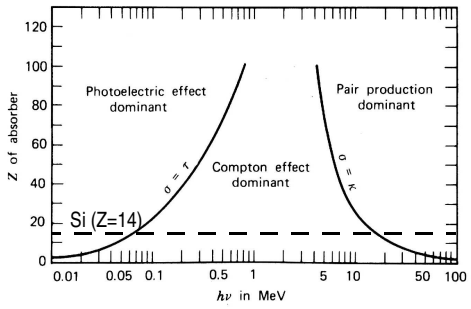

Figure 5-2: The importance of the three different photon interactions for different atomic number Z as a function of photon energy. The solid lines indicates the energy where the interactions on both sides of it are equally probable to take place and the dashed line indicates Si (Z=14) .

In Compton scattering, the energy of the photon is much greater than the binding energy of the atomic electrons (such as those in the K shell). The incident photon transfers a fraction of its energy to scatter an atomic electron, thereby creating an energetic Compton electron.

Unlike photoelectric effect, where the initial photon was absorbed, the scattered photon continues to traverse the target material, where it can undergo further Compton scattering if the energy is sufficient. As the photon energy increases, Compton scattering dominates over the photoelectric effect.

The third type of photon interaction, pair production, has a threshold energy of 1.02 MeV (2×the rest mass of an electron/positron). At this energy, a photon striking a high–Z target will be completely absorbed and cause a positron–electron pair to form.

As illustrated in Figure 5-2, for silicon (Z=14), the photoelectric effect is dominant at energies below 50 keV. Above 20 MeV pair production is the most probable interaction. Compton scattering dominates in the intermediate energy range.

Charged Particles

Heavy charged particles incident on matter interact primarily by Coulomb scattering. In the inelastic case, energy is transferred from the particle to the orbital electrons in the atom causing an ionization (electron–hole pairs in semiconductors) or excitation. The amount of energy transferred in each collision is typically a very small fraction of the particle's kinetic energy; however, in normally dense matter, the number of collisions per unit path length is so large, that a significant energy loss is observed even in relatively thin layers of material.

The inelastic collisions are statistical in nature, occurring with a certain quantum mechanical probability. However, when considering macroscopic distances, the number of collisions per path length is very large. Therefore the fluctuations in the total energy loss are small and one can use the average energy loss per unit path length in many calculations. This quantity, often called the *stopping power* or *dE/dx*, was first calculated by Bohr using classical arguments and later by Bethe, Bloch and others using quantum mechanics.† For a particle with charge *ze*, velocity *v* and rest mass *m*, the stopping power is described by the *Bethe–Bloch formula*:

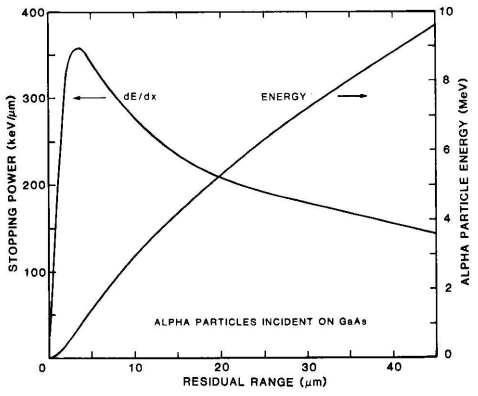

Figure 5-3: Energy dependence of the total stopping power and range for alpha particles incident on GaAs [31].

$$\frac{dE}{dx} = -4\pi \cdot \frac{e^4 z^2}{mv^2} \cdot NZB \qquad (5\text{-}1)$$

N and *Z* denotes the atomic density and atomic number of the target material. The *B* factor depends logarithmically on v^2. Thus, the general dependence of *dE/dx* on the particle velocity can be inferred from the factor containing $1/v^2$. Since the energy of a non–relativistic particle is proportional to v^2, the Bethe–Bloch formula express that low–energy particles lose

† Stopping power is sometimes referred to as the Linear Energy Transfer (LET). There is a slight difference though: LET takes into account only the energy deposited locally along the particle trajectory, whilst stopping power refers the total energy lost by the incident particle, including energy lost by radiation of bremsstrahlung–photons that sometimes deposit their energy far from the actual trajectory.

energy at a much greater rate than high–energy particles. Figure 5-3 shows the stopping power versus residual range for alpha particles incident on GaAs [31]. As an example, the range of a 5 MeV alpha particle is 18.5 µm and dE/dx=216 keV/µm initially. As the particle slows down along its track due to energy loss, dE/dx increases to a peak at ~1 MeV and then decreases sharply

5.2.2 Non–Ionising Interactions

Neutrons

Since neutrons are neutral, they don't interact with the atomic electrons. Instead they interact directly with the nucleus. The interaction can be either inelastic or elastic.

Elastic neutron interaction (n,n) means that the neutron is captured by the target nucleus and subsequently reemitted with the same energy. Inelastic reactions (n,n') involves capture of the neutron by the nucleus, followed by emission of a neutron at a lower energy. Kinetic energy is lost in this process, and the nucleus is left in an excited state. The excited nucleus returns to its original state by emission of a gamma ray. The kinetic energy of the emitted particle is reduced, compared to the incident particle, by the energy of the gamma ray. Inelastic scattering can also cause displacement of the target atom to occur.

Another type of reaction, called transmutation, involve capture of the incident particle by the target nucleus and subsequent emission of another type of particle. The remaining atom is thereby converted from one element to another. Examples of transmutation interactions are: proton production (n,p) and alpha–particle production (n,α). These two reactions can also occur with an additional neutron in the final state, which is denoted (n,pn) and (n,αn).

In all these processes a nuclear recoil is produced, which can be treated as a heavy ion incident on a silicon target. The recoil subsequently loses its energy to ionization and to further displacement of atoms and nuclei. The cross–section for the 6 processes mentioned above have a threshold energy of a few MeV in silicon. However, sometimes boron is used as a dopant in the fabrication of semiconductors. Boron has a large capture cross–section for thermal neutrons and can therefore cause heavy recoils to be produced.

Charged Particles

As a result of Columb scattering, a substantial amount of energy can be transferred to the whole target atom. The displaced atom is referred to as the primary recoil (or primary knock–on). It subsequently will lose energy to ionization, but can also displace other lattice atoms (a process that can occur as long as the transferred energy is greater than that required for displacement). Heavy charged particles can also undergo nuclear interactions similar to neutrons, which include elastic scattering, inelastic scattering and transmutation.

5.3 Displacement Damage in Semiconductors

5.3.1 General Considerations

A well understood behaviour of semiconductors is that impurity atoms in the silicon lattice introduce energy levels in the bandgap between the conduction band and the valence band that have a major impact on the electrical behaviour of semiconductor devices. However, in principal any disorder in the lattice structure can generate energy levels in the bandgap. Radiation–induced defects have such energy levels associated with them.

Different types of defects can occur in a semiconductor exposed to radiation. One can classify them as *i*) simple displacements where only one atom is involved (referred to as point, or isolated, defects) and *ii*) cluster effects that can occur when an atom is given a large amount of kinetic energy by an incident particle. The primary knock–on can then displace many other atoms, and thereby cause the creation of disordered regions. This process can also occur for incident neutrons with energy in the MeV range. Electrons and photons with this energy mainly produce isolated defects. Figure 5-4 shows three effects, and their consequences, that can result from radiation–induced defect centres in the semiconductor bandgap.

- Process 1 is due to induced energy levels near the middle of the bandgap. Thermal generation of electron–hole pairs through this level is then enhanced. This effect is important in the depletion region since the electrons and the holes are quickly swept away by the strong electric field in that region. Such defects cause an increase of leakage current in silicon devices.
- Process 2 is the recombination of electron–hole pairs. As opposed to the generation process, recombination *removes* electron–hole pairs. The mean time a minority carrier† spends in its band before recombining is referred to as the recombination lifetime, τ_r. Radiation–induced recombination centres cause τ_r to decrease. This is the dominant mechanism for gain degradation in bipolar transistors.
- Process 3 is the temporary trapping of carriers at a typically shallow level. In this process, a carrier is captured at a defect centre and is later emitted to its band, with no recombination event taking place.

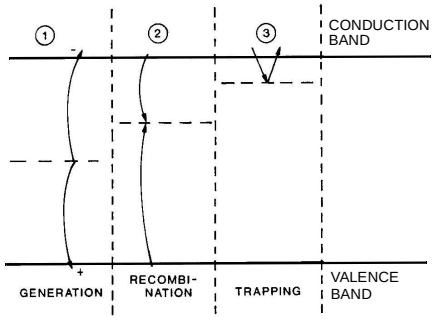

Figure 5-4: Three effects that can occur due to the presence of defect centres in the silicon bandgap [31].

The rate at which electrical properties of electronic materials degrade in a radiation environment is often expressed in terms of damage coefficients. For example, minority–carrier recombination lifetime degradation can be expressed as

$$\frac{1}{\tau_r} = \frac{1}{\tau_{r0}} + \frac{\phi}{K_r} \qquad (5\text{-}2)$$

† A minority carrier is an electron on the a p–doped side, or a hole on the a n–doped side, of the depletion region.

In this equation, τ_{r0} and τ_r, are the pre– and post–irradiation values of lifetime, ϕ is the particle fluence, and K_r is the recombination lifetime damage coefficient. Similar expressions can be written for generation lifetime, diffusion length, and carrier mobility. For radiation–induced compensation, the decrease in carrier concentration is characterized by a carrier removal rate. In silicon, the damage coefficients typically depend on particle type and energy, material type, resistivity, impurity substance and concentration, temperature, and time after irradiation.

5.3.2 Annealing

Damage to the lattice structure in a material normally disappear when the material is heated. This effect is called “annealing”. Annealing can partially or totally re–settle the electrical and optical properties that a semi conducive material has lost due to radiation. as a device often is operated at sufficient annealing temperatures annealing can take place at same time as radiation damage.

5.3.3 Displacement Damage in GaAs VCSELs

As discussed previously, VCSELs emit light through stimulated radiative recombination of excess carriers across a p–n junction. A fraction of the carriers recombine non–radiatively through centres in the bandgap. In an efficient VCSEL, radiative recombination is however the dominant mechanism by which carriers recombine. In general, radiation that causes displacement damage in a VCSEL will introduce nonradiative recombination centres, and thus degrade the light output. This is the dominant permanent effect of radiation on VCSELs.

Displacement damage can also cause an increase in the threshold current I_{th}. This effect correlates with a decrease in electroluminescent efficiency (or quantum efficiency), which is the fraction of the total number of recombinations which are radiative, and is attributed to the introduction of nonradiative recombination centres.

In general, laser diodes operated under high current conditions (i.e., well above I_{th}) are relatively insensitive to irradiation. Lasers should be selected that have a low I_{th} and a high allowable operating current.

VCSELs show a higher degree of radiation tolerance than LEDs. This is due to the fact that the lifetime of the minority carriers are governed by *stimulated* emission, which makes it several orders of magnitudes smaller than for LEDs. Also the active region is much smaller than in LEDs.

5.3.4 Displacement Damage in Bipolar IC circuits

For bipolar integrated circuit technologies, such as ECL and TTL, radiation–induced recombination in the base region can contribute to gain degradation. In addition, use of a heavily–doped shallow emitter in ECL and TTL circuits substantially reduces radiation–induced recombination in the emitter.

Displacement damage also gives rise to generation centres, and such centres can play an important role in the reverse–biased base–collector junction. The reverse leakage current at that junction will increase due to the thermal generation of electron–hole pairs at radiation–induced centres, and the subsequent sweep–out of these carriers by the high field present. Leakage current can also increase due to generation centres produced at the surface by ionizing radiation.

In general, the regions of bipolar transistors in an integrated circuit depends on device and circuit structures and geometries. Therefore, these effects are very hard to generalise and need to be investigated by performing irradiation studies of every separate device.

5.4 Radiation Effects in Optical Fibres

Typically, ionising radiation will dominate over displacement effects in producing increased photo absorbtion by the trapping of electrons and holes, generated by the ionizing particles, at pre–existing sites. This process constitutes “colour centre” formation.

Fibres that contain relatively few impurities will have a reduced radiation response (e.g. pure silica core fibres). Fibre production conditions [32], including the level of phosphorus doping† in particular [33], can strongly affect the radiation tolerance of a given fibre. Figure 5-5 illustrates the radiation induced coloration in a germanium doped silica fibre.

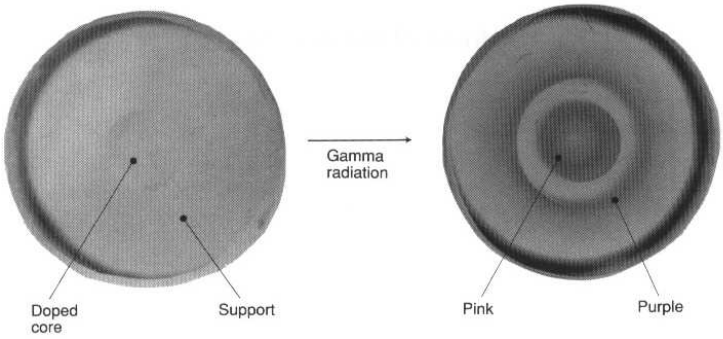

Figure 5-5: Coloration in a Germanium doped silica fibre [34].

In general there is a level of annealing in optical fibres. The speed of this annealing is influenced by factors like temperature, light intensity and light wavelength. The annealing can be strongly influenced by the presence of impurities in the fibre core. Phosphorus acts to inhibit annealing. Thus phosphorus doped fibres are often observed to have poor radiation tolerance.

5.5 Single–Event Effects

A Single–Event Effect (SEE) result from a single, energetic ionising particle. SEEs can be classified into three groups (in order of permanency):

- Single-event upset (soft error)
- Single-event latchup (hard error)
- Single-event burn–out (hard error)

Since this work only concerns single-event upsets, this type of failure is described in some

† Phosphorus acts to inhibit annealing of optically active defects and this is the origin of the observed poor radiation tolerance of optical fibres with phosphorus doping.

detail below. The two other effects are described briefly at the end of the this chapter.

5.5.1 Single Event Upset

Single-event upsets or SEUs are an important problem for digital integrated circuits in a radiation environment. A single high–energetic particle (typically a knock–on Si–ion recoil) striking an integrated circuit element will lose energy via the production of electron–hole pairs, resulting in a ionized track in the region of that element. The released charge can then be collected at a circuit element and cause the value of a logical state to be altered.

Figure 5-6a shows the simple example case of a particle normally incident on a reverse–biased p–n junction. Charge collection occurs by three processes which begin immediately after creation of the ionized track: drift in the equilibrium depletion region, diffusion, and funneling. A high electric field is present in the depletion region, so carriers generated in that region are swept away. With a depletion region width of 1 µm, carriers will be swept away in a time on the order of 10^{-11} s for a GaAs device [31]. Carriers generated beyond the depletion region width can be collected by diffusion, particularly when the end of the track is in the region within a diffusion length L of the depletion region edge. The time scale for charge collection via diffusion is of the order of several minority–carrier lifetimes.

A third process, called “funneling”, also plays an important role in the collection process. Charge funneling involves a spreading of the field lines into the device substrate beyond the depletion width, sometimes causing charge to be pulled back up the track toward the silicon surface rather than diffusing into the silicon bulk (illustrated in Figure 5-6a). This greatly increased the SEU rate of circuits. The time scale for charge collection via funneling is on the order of 0.1 ns [31]. Figure 5-6b shows the resulting current pulse that is expected to occur due to the three charge collection processes described above. Reference [35] describes measurements of the single–particle–induced current pulse.

The magnitude of the current pulse determines whether upsets occur in such circuits. In general, it is important to note that SEUs occur in various types of integrated circuits, including memories, microprocessors, and logic circuits. The circuit–specific mechanism responsible for SEU can be complex and needs to be examined and understood for every separate case.

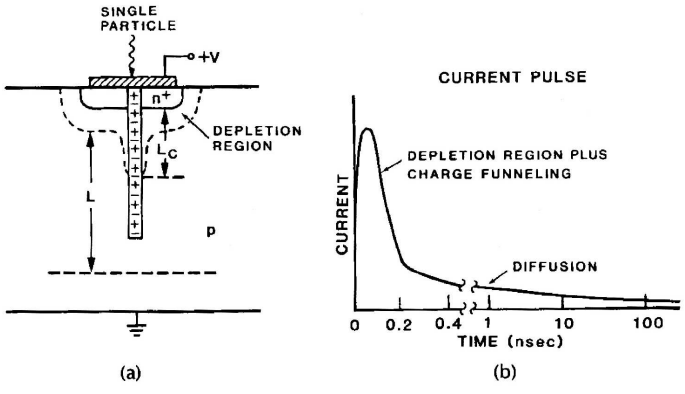

Figure 5-6: The charge collection mechanism that cause single–event upsets [31].

5.5.2 Neutron Induced SEUs

In the discussion about neutron interactions with matter (Chapter 5.2) it was said that a typical process involves the capture of the neutron and a subsequent emission of heavy particle like a neutron, proton or alpha particle, often accompanied by a gamma photon from nuclear deexcitation. Protons and alpha particles could in principle cause a SEU according to the mechanism described in above. However, this is believed to be a secondary effect; more important is the nuclear recoil which can be treated as a highly charged heavy ion† [36], which according to the Bethe–Bloch formula (Equation 5-1), will deposit a large amount of energy in a small region.

Burst Generation Rate (BGR)

The concept of BGR was developed to calculate the rate of SEU induced by protons and neutrons in silicon via the energy deposition from the resulting nuclear reaction products [36]. The calculation makes use of silicon cross–section data and involves energy transport Monte Carlo simulations.

The differential cross–section for a neutron with energy E_n to interact, by a nuclear process i, and cause a nuclear recoil of energy E_r in the direction θ is given by $d\sigma^i/d\Omega(\theta, E_r, E_n)$. Not all recoils have a direction or enough energy to deposit enough charge at a sensitive node to cause a SEU. Thus, to get the total cross–section σ_{burst} for producing recoils that can do this, one have to integrate over some critical part of the total solid angle Ω_c and over the part of the recoil energy spectrum that lies above some critical threshold energy E_c, according to:

$$\sigma^i_{burst}(E_c, E_n) = \int_{E_c}^{\infty}\int_{\Omega_c} \frac{d\sigma^i}{d\Omega}(\theta, E_r, E_n) dE_r d\Omega \qquad (5\text{-}3)$$

The Burst Generation Rate (BGR) is then defined as,

$$BGR^i(E_c, E_n) \equiv \rho_A \sigma^i_{burst}(E_c, E_n) \qquad (5\text{-}4)$$

where ρ_A denotes the atomic density in the material. The name “rate” is misleading because this is really the probability per unit path length (and unit neutron flux since it is a cross–section) for a neutron with energy E_n to produce a nuclear recoil with energy $E_r > E_c$.

The HETC Monte Carlo code [37] combined with evaluated nuclear data from the ENDF/B–VI [37] neutron cross–section database has been used by others [38] to calculate $\rho_A \sigma^i_{burst}$ for a number of different nuclear reactions. In Figure 5-7 [38] this quantity is shown for the six nuclear interactions believed to be of most importance for generation of SEUs. The value of E_c is equal to 0.675 MeV‡ in these calculations. An important feature of these curves is that they all have a threshold above ~5 MeV, which means that, according to this model, no SEUs should be generated by neutrons below this energy.

The total burst generation rate is just the sum of the contributions from the different processes

† Since it gets stripped of most its electrons.

‡ A somewhat arbitrary choice by the authors of [38].

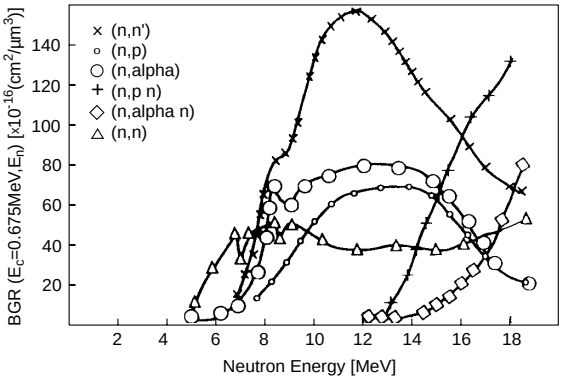

Figure 5-7: BGR curves for the six nuclear processes believed to be of most importance for the generation of SEUs in silicon [38].

$$BGR(E_c, E_n) = \sum_i BGR^i(E_c, E_n) \qquad (5\text{-}5)$$

To calculate the rate R_{burst} at which these bursts are generated one must multiply with the neutron flux dN/dE_n by taking the convolution according to:

$$R_{\text{burst}}(E_c) = \int_0^\infty BGR(E_c, E_n) \times \frac{dN}{dE_n} dE_n \qquad (5\text{-}6)$$

Often it's more convenient to work with spectra that are normalised to unit area according to

$$\int_0^\infty \left(\frac{dN}{dE_n}\right)^{norm} dE_n = 1 \qquad (5\text{-}7)$$

For a non–normalised spectrum one have the following relation:

$$\int_0^\infty \frac{dN}{dE_n} dE_n = \phi \qquad (5\text{-}8)$$

where ϕ is the total neutron flux. Equation 5-6 to 5-8 then gives

$$R_{\text{burst}}(E_c) = \phi \times \underbrace{\int_0^\infty BGR(E_c, E_n) \times \left(\frac{dN}{dE_n}\right)^{norm} dE_n}_{\equiv \int BGR(E_c)} \qquad (5\text{-}9)$$

where the symbol $\int BGR(E_c)$ is defined to denote the convolution between the BGR curve for the nuclear recoil E_c and the normalised neutron spectrum

The expression in Equation 5-9 has the dimension $s^{-1}cm^{-3}$. Thus, this is the burst rate per cm^3. If the whole chip were "sensitive", in the sense that a SEU would occur every time a burst was generated anywhere in the chip, one could calculate the actual SEU rate R_{SEU} by mul-

tiplying by the total volume of the chip. But since only some parts of the silicon (where the sensitive components are positioned) are relevant, one instead multiply by a factor εV, where V is the total sensitive node volume and ε is a dimensionless collection efficiency factor needed to compensate for the fact that some of the generated charge escape from V. The actual SEU rate, R_{SEU} is thus proportional to $\int BGR(E_c)$ according to:

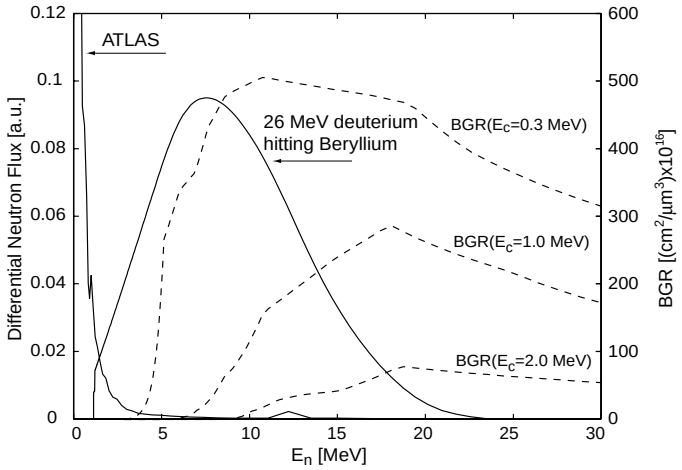

Figure 5-8: Three BGR curves plotted as a function of neutron energy. These are overlaid by the simulated ATLAS neutron spectrum and the spectrum obtained when a 26MeV deuterium beam is collided with a Beryllium target. The ATLAS spectrum appears not to be normalised when compared to the other one, but this is an artifact of the y–axis cut–off at 0.12 above which the spectrum rises extremely steeply.

$$R_{\mathrm{SEU}}(E_c) = \varepsilon V \times \phi \times \int BGR(E_c) \qquad (5\text{-}10)$$

In Figure 5-8 $BGR(E_c, E_n)$ taken from reference [39] has been plotted for three different E_c values. A large value of E_c means that the nuclear recoil energy must be large to cause a SEU–generating burst. This explains the increase in BGR threshold for increasing E_c. In addition to this, two normalized differential neutron spectra are plotted. One spectrum is the simulated spectrum in ATLAS, and the other is obtained when a 26MeV deuterium beam is collided with a Beryllium target. Since a larger fraction of latter overlaps with the BGR curves, one should, following the discussion above, get a higher value of $\int BGR(E_c)$ and, therefore according to Equation 5-10, a higher value of $R_{\mathrm{SEU}}(E_c)$.

5.5.3 Single–Event Latchup

Single-event latchup (SEL) is a condition that causes loss of device functionality due to a single-event induced current state. SELs are hard errors, and are potentially destructive (i.e., may cause permanent damage). The SEL results in a high operating current, above device specifications. The latched state can destroy the device, pull down the bus voltage, or damage the power supply. Typically, latchup is caused by heavy ions, however, it can be also be caused by protons in very sensitive devices. An SEL is cleared by a power reset of the device. If power is not removed quickly, destructive failure may occur due to excessive heating, or bond wire failure.

5.5.4 Single–Event Burnout

Single-event burnout (SEB) is a condition that can cause device destruction due to a high current state in a power transistor. SEB causes the device to fail permanently. They include burnout of power MOSFETs, gate rupture, frozen bits, and noise in CCDs (charge-coupled devices). Only SEB of n-channel power MOSFETs has been reported. An SEB can be triggered in a power MOSFET biased in the OFF state (i.e., blocking a high drain-source voltage) when a heavy ion passing through deposits enough charge to turn the device on. SEB susceptibility has been shown to decrease with increasing temperature.

–♦–

CHAPTER 6

TOTAL DOSE STUDIES

In this chapter a series of total dose radiation tests with neutron and gamma radiation, performed at a few different locations in Sweden and France, are described. The induced attenuation of VCSELs and optical fibres have been measured along with functional tests of the G–link seialiser chip. The results presented in this chapter are summarised in two papers submitted to Nucl. Instr. and Meth. A [3], [4]

6.1 Introduction

It is crucial that the behaviour of the optical link components is well understood under the radiation conditions that will prevail in ATLAS, especially as access is limited once the detector is closed. As discussed previously, integrated over 10 years of LHC running (3 years at $10^{33}cm^{-2}s^{-1}$ and 7 years at $10^{34}cm^{-2}s^{-1}$), the expected doses are ~800Gy(Si), ionising; and 1.7×10^{13} n(1MeV(Si))/cm^2. It is therefore essential to perform radiation tests with the aim of looking for permanent damage effects like:

- light power attenuation of VCSELs and destruction of packaging†
- threshold–current movement of VCSELs
- induced attenuation of the glass lens in the TO–46 package
- induced attenuation of optical fibres
- functional failure of the G–link serialiser

and if damage is seen:

- possible annealing behaviour.

6.2 Test Facilities

6.2.1 Neutron Irradiation

SARA

The SARA‡ cyclotron system is located at ISN in Grenoble. Neutrons were produced by impinging a 20MeV deuteron beam on a 3mm thick beryllium target 3.5cm in diameter. A stripping reaction ($^9Be(d,n)^{10}B$) takes place which gives a continuous neutron energy spectrum covering energies up to 25MeV with a mean energy of 6MeV (see Figure 6-1a). The neutron flux is proportional to the incident beam current with a neutron yield of $\sim5\times10^7$n/(nA·s·sr). Thus, at 10cm from the target, a beam current of 2µA gives a flux of the order 10^9 n$cm^{-2}s^{-1}$. Since a cryostat filled with liquid argon (used for other tests) is positioned in front of the beryllium target, the neutron flux is attenuated by a factor of about two [41].

The neutron beam also contained some gamma radiation, associated with the nuclear reac-

† As gamma radiation only cause ionisation, there is no theoretical reason to suspect that it should cause light power degradation of VCSEL emitters. However, the plastic lens in the TO–46 package might be damaged and thereby inducing a decrease in the light power output.

‡ SARA stands for Système Accélérateur Rhône–Alpes. The facility was shut down in 1999. A description of the neutron facility is found in [40].

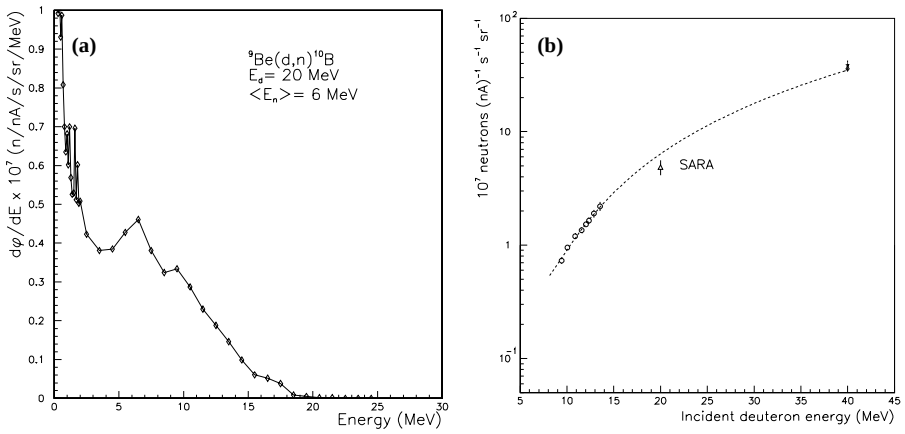

Figure 6-1:
a) The neutron spectrum at SARA. The method used to measure this spectrum a is based on a TOF technique, where NE213 scintillators were used. This introduce a cutoff at around 1MeV [40].
b) Neutron Yield for the ^{9}Be(d,n)^{10}B reaction in a "thick" beryllium target as a function of deuterium energy.

tions in the target. However, the amount of this contamination was not easily measured at the position of the devices under test (DUT), using alanine dosimeters†, as they are also affected by the neutrons. A previous study showed that for a fluence of 3×10^{14}n(1MeV(Si))/cm^2 the ionising dose measured at the target is 3.3kGy(Si) [40]. The presence of the liquid argon cryostat means that the ionising dose received by the DUT can be considered to be negligible at the fluences in question, as it is absorbed by the liquid argon.

Unlike the ATLAS radiation environment, no thermal neutrons are produced in the stripping process. Thus, as discussed in Chapter 5.5.2, the tests performed with this neutron spectrum is insensitive to the potential damage mechanisms (and/or generation of SEUs) that could occur due to the presence of boron dopants [42]. Nevertheless, the lack of thermal neutrons had the advantage that the activation of the devices under test was limited so that one had access to them within a week after the irradiation.

The activation of nickel foils, placed on the devices under test, was used to determine the absolute neutron fluence (for neutrons with energies above ~100keV). Due to the charge exchange reaction ^{58}Ni(n,p)^{58}Co, the neutron fluence could be deduced by measuring the activity of the ^{58}Co. This was done after the end of the irradiations to an accuracy of around 15%. The kerma factors used to convert the fluence from the actual energy spectrum in Figure 6-1a, to 1MeV equivalent fluence, was 2.3±0.3 for GaAs and 1.5±0.2 for silicon.

CERI

CERI‡ lies in Orlean south of Paris. It is a centre for medical radiation physics. The neutron production mechanism and dosimetry is the same as at SARA§ but the energy of the incident

† Alanine is an amino acid that, under influence of radiation, produces free radicals in proportion to the absorbed dose. The concentration these is then measured by means of EPR (Electron Paramagnetic Resonance).

‡ Centre d'Etudes et de Recherches par Irradiation.

§ The Be–target used at SARA was moved to CERI.

deuteron beam is tuneable in the range 5–25 MeV. As at SARA, a fixed incident beam energy gives a neutron flux that is proportional to the incident beam current. The neutron yield (and therefor the flux) depends on the deuterium energy according to Figure 6-1b. In contrast to the SARA facility there is no cryostat in front of the target, which resulted more gamma–background. The neutron energy spectrum for a few typical deuteron energies are illustrated in Figure 6-2†. Figure 6-3a shows the target area at CERI.

Chalmers

Chalmers is a technical university in Göteborg. The neutron generator was provided by the Department of Reactor Physics. It consists of an ion source, accelerator tube and a target. Deuterium ions are injected into the accelerator tube by the ion source and accelerated along the tube using a potential difference of 300 kV. The deuterium ions hit a deuterium or tritium target. The reactions yield a neutron spectrum narrowly peaked at 2.45 MeV for the $^{2}H(d,n)^{3}He$ reaction and 14.1 MeV for the $^{3}H(d,n)^{4}He$ reaction. The flux was monitored in real time using a calibrated neutron counter (a plastic scintillator) placed 1 m from the target. The gamma contamination in the neutron beam was negligible [43].

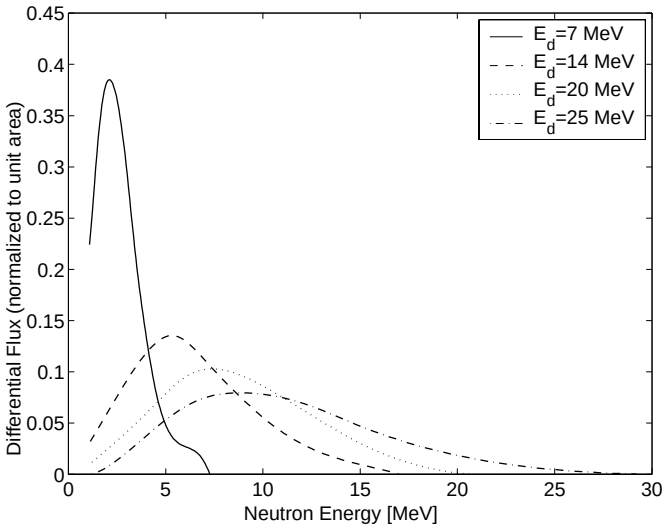

Figure 6-2: Neutron spectra for deuterium with different energies impinging on a beryllium target [44].

6.2.2 Gamma Irradiation

Karolinska

Karolinska is a hospital in Stockholm. The gamma irradiation facility is normally used as a gamma treatment facility (see Figure 6-3b). The source consists of ^{60}Co which upon decay emits two gamma rays at energies 1.17 and 1.33 MeV. The integrated ionising dose, received by the components, was measured with alanine dosimeters with an accuracy of

† The neutron spectrum for E_d=20 MeV differs significantly from the one in Figure 6-1 for neutron energies below ~5 MeV. This difference is not fully understood but may be due to differences in measurement techniques. The discrepancy does not have any implication on the results quoted in this work, as the spectra in this figure only will be used in a situation (next chapter) where the higher part of the energy spectra (which is in good agreement with the one in Figure 6-1) is relevant.

around 4%. As a cross check a direct measurement was performed with a silicon diode dosimeter before and after the test.

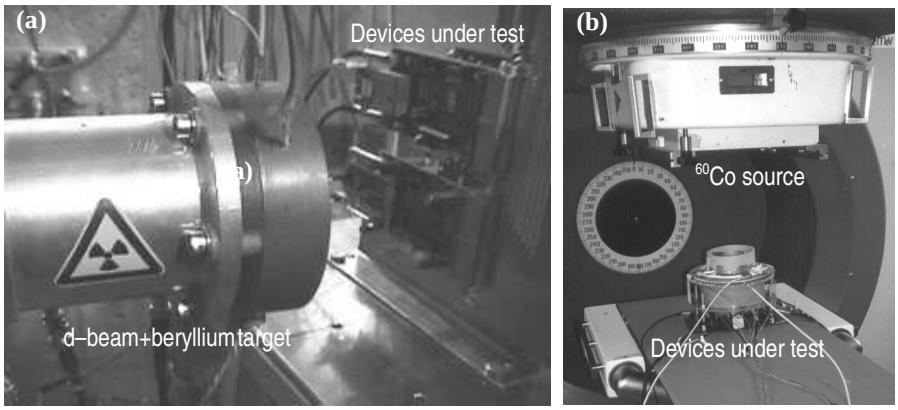

Figure 6-3: a) The target area at the CERI neutron irradiation facility. b) The ^{60}Co source at Karolinska hospital.

6.3 VCSEL irradiation

Nine VCSELs from Honeywell® [45] and nine from Mitel®† [46] were exposed to neutron and gamma radiation, and measurements were performed to determine if the light output power and/or the threshold current of the VCSELs changed during irradiation.

The TO–46 packages from Honeywell were equipped with a glass lens to allow for efficient optical coupling into the fibre whilst the Mitel packages had a flat glass window in place of a lens which consequently led to less efficient coupling to the fibre. The TO–46 packages were mounted inside metal ST connectors to provide easy connection to the fibres.

6.3.1 Experimental Procedure

During both the neutron and the gamma irradiations the VCSELs were placed in the radiation field on two closely spaced FR4 motherboards. Each motherboard contained a mixture of both VCSEL types. The Honeywell VCSELs will be referred to as H1–H9 and the Mitel VCSELs as M1–M9. Current was fed to each VCSEL anode from a GPIB controlled current source through a relay–based demultiplexer. The VCSEL cathodes were connected to a common ground. Each VCSEL was coupled to an optical fibre via an ST connector, and the fibre was routed to the control room where it was coupled to an 8 channel PIN–diode array with attached transimpedance amplifiers [47].

The outputs from the amplifiers were connected to a 12 bit ADC mounted inside a PC. The current source, demultiplexer, and ADC were controlled by the PC which ran LabView‡ software to allow for automated testing. The fibres were routed in a way to minimize the exposure to the radiation field§, and thus minimize possible radiation–induced attenuation.

Periodically during irradiation (every 20 minutes for the first few hours and then once per

† The part number was HFE4080–321 (Honeywell) and from 1A440 (Mitel) VCSELs.

‡ LabView is a data acquisition and instrument control software from National Instruments®.

hour) a VCSEL was selected and biased between 0–10 mA in 20 equally spaced steps. At each step, the current was applied for 1 s before an ADC reading was taken. Each ADC measurement consisted of 100 samples taken at 1 kHz. When one VCSEL was selected in this way, all the other VCSELs were biased with a constant current. The nominal bias values were 7 mA for H1–H5, 8 mA for H6–H9, 5 mA for M1–M5 and 6 mA for M6–M9. All of these bias currents are above lasing threshold. About 10 minutes was needed to measure all of the VCSELs in this way.

After the irradiation, the measurement procedure continued in order to check for possible annealing effects. After the neutron irradiation, the components were left untouched for 84 hours during these tests. This was not an option after the gamma irradiation but the tests were carried on, after the set–up was relocated to KTH, for a period of 90 hours.

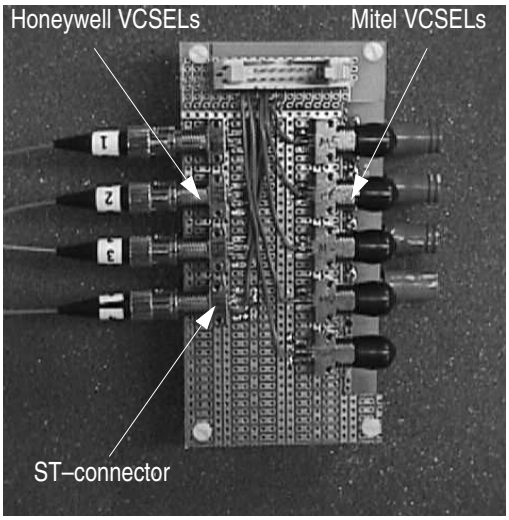

Figure 6-4: The FR4 motherboard with four Honeywell and 5 Mitel VCSELs in ST housings.

6.3.2 Irradiation Details

Neutrons

The VCSELs were first irradiated with neutrons at the SARA facility. The exposed components were located approximately 30 cm from the target, behind the cryostat filled with liquid argon. A total neutron fluence of $(2.10\pm0.41)\times10^{13}$ n(1 MeV(GaAs))/cm^2 was generated in approximately 35 hours, which corresponds well to the fluence expected after 10 years of LHC running. The instantaneous flux is thus ~800 times larger than at ATLAS.

Gamma

At the gamma irradiations, performed at Karolinska, a total dose of 5.1±0.2 kGy(GaAs) was delivered to the components in approximately 70 hours. This corresponds to about 65 years of LHC running.[†]

§ This test was carried out using a fibre from Acome®. In Section 6.4 it is shown that this fibre is not particularly radiation tolerant, but since the section of the fibre exposed to radiation was very short (~10 cm), this effect is negligible.

6.3.3 Results

Neutrons

Figure 6-5 a shows the relative attenuation of the light output from a typical Honeywell VCSEL as a function of time. This plot is typical for each Honeywell VCSEL and consistent behaviour is seen for all the Mitel VCSELs. As the plot illustrates, there is an immediate attenuation of 5–10% at the start of the irradiation, which is followed by a slight increase in attenuation during the course of the irradiation. At the end of the irradiation a 90 hours long annealing process returns the light output to better than 95% of the pre–irradiation level.

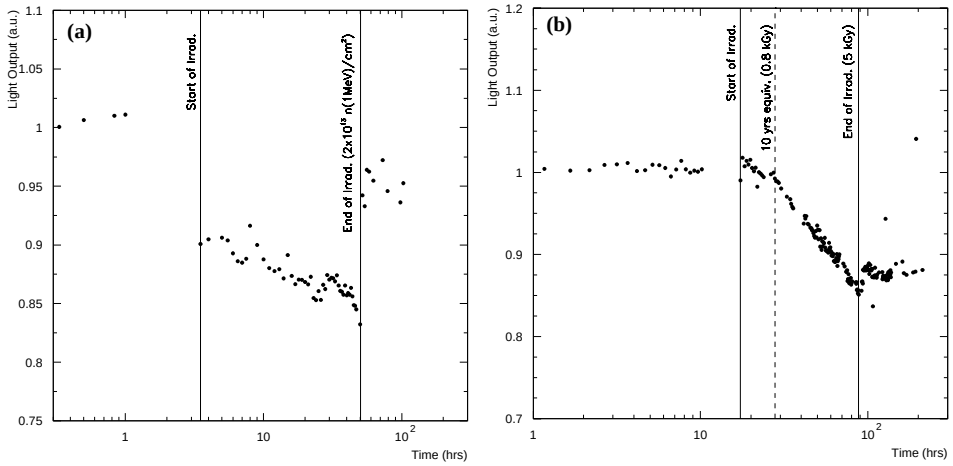

Figure 6-5:
a) Relative attenuation of the light output from a typical Honeywell VCSEL as a function of the time during a neutron irradiation. Note the annealing behaviour after the irradiation is completed.
b) Relative attenuation of the light output from a typical Mitel VCSEL as a function of the time during a gamma irradiation. Note the absence of annealing after the irradiation is completed. The dotted line denotes a 10 year LHC equivalent dose. The two atypical points seen in the annealing phase are spurious.

The light output attenuation observed for the Honeywell VCSEL is consistent with that seen in earlier neutron irradiation studies of a prototype version of this device tested at cryogenic temperatures [23].

Gamma

Figure 6-5b shows the corresponding results from the gamma irradiation of a typical Mitel VCSEL. The Honeywell VCSELs showed a similar behaviour. The attenuation characteristics is noticeably different compared to the neutron results. The light output attenuation is here proportional to the accumulated dose. The dotted line indicates the dose expected after 10 years of LHC running. The scatter of the points for the Mitel VCSEL appears smaller than for the Honeywell VCSEL due to the resolution of the ADC and the received power for the Mitel VCSELs being approximately 10 times smaller than that for the Honeywell VCSEL due the absence of a coupling lens. After the irradiation there was no evidence for any significant annealing in any of the VCSELs.

Light output attenuation of VCSEL emitters due to gamma irradiation is not supported by

† The length of this test was dictated by access schedules to the irradiation facility.

the theory in Chapter 5. The appearance of attenuation in this particular test is somewhat unclear, but the absence of annealing suggests that the measured effect is due to degradation of other parts of the system. As mentioned, the fibre attenuation is thought to be negligible, but nothing is known about the ionising–radiation effects on the glass window in the T0–46 package. Nevertheless, the attenuation after the equivalent 10 year dose was <5% for all VCSELs.

The threshold current for either type of VCSEL did not move significantly during either type of irradiation. Furthermore, the induced attenuation and annealing behaviour for either brand of VCSEL showed no bias current dependence.

6.4 Fibre Irradiation

Two standard "off the shelf" optical fibres supplied by Acome® [48] and Plasma Optical Fibres® (POF) [49] were tested with neutron irradiation. The Acome fibre was subsequently also tested with gamma. Both fibres had a GRIN doping profile. The POF fibre has a germanium doping in the core. It is therefore thought to show improved radiation tolerance compared to the Acome fibre which apart from germanium had an additional phosphorus doping (see Chapter 5.4). In both fibres a pure silica cladding extends up to a diameter of 125 µm. The fibre is then coated with acrylate to give it an overall diameter of 250 µm. The properties of the fibres are summarised in Table 6-1.

	POF	**Acome**
Configuration	50/125	50/125
Doping profile	GRIN	GRIN
Core dopants	Ge	Ge,P
Cladding dopants	None	Unknown

Table 6-1: Summary of properties for the irradiated fibres.

6.4.1 Experimental Procedure

The characteristics of the gamma and neutron irradiation tests are summarised in Table 6-2. The light in the fibre under test (FUT) was provided by VCSELs operating around 850 nm. Measurements were made in two different ways, denoted "manual" and "auto" in the table. With the manual method light was measured "by hand", using a light power meter, at a number of times during the irradiation, This required optical connections to the FUT to be manipulated during the irradiation. With the automatic method this was not necessary as the FUT were continuously connected to the measurement apparatus and could therefore be left untouched during the test. In this kind of arrangement the light power was measured with means of the same PIN–diode arrays (+transimpedance amplifiers), used in the VCSEL test described above. Also here the data acquisition consisted of a PC running LabView.

For both methods the FUT was mounted inside the irradiation chamber through–out the whole measurement period. In all cases, fibres used to transfer power to and from the FUT were not exposed to significant levels of radiation.

6.4.2 Irradiation Details

Neutrons

The neutron tests were preformed at the SARA facility. The fibres were placed 30 cm down-

	Gamma	Neutrons	
	Acome	*Acome*	*POF*
Form[a]	Ribbon (4/8)	Ribbon (2/8)	Duplex
Total length (m)	10	10	7
Spool Diameter (cm)	10	8[b]	8[b]
Facility	Karolinska	SARA	SARA
Dose	4.9 kGy(Si)	3×10^{12} n(1MeV(Si))/cm^2	3×10^{12} n(1MeV(Si))/cm^2
Dose rate	72 Gy(Si)/h	9.7×10^{10} n(1MeV(Si))/cm^2/h	7.6×10^{10} n(1MeV(Si))/cm^2/h
Dosimetry	alanine	Ni foil	Ni foil
Test	Automatic	Automatic	Manual
Test power (μW)	700	600	500

Table 6-2: A summary of the gamma and neutron irradiation studies.

a. "Ribbon (4/8)" means that the fibre was formed into 8–way ribbon of which only 4 were used for measurement.
b. This diameter was chosen to match the size of the neutron field.

stream from the target behind the cryostat filled with liquid argon. At this position, the neutron flux is approximately maximal and homogeneous across a disk of 8 cm in diameter centred on the beam axis. The fibres were exposed to a total fluence of 3×10^{12} n(1 MeV(Si))/cm^2.

Gamma

During the gamma irradiation a total dose of 4.9 kGy(Si), corresponding to approximately 60 years of LHC running, was delivered to the FUT in approximately 70 hours. The irradiated part of the fibre was 10 m long winded on a cylinder with a diameter of 10 cm.

6.4.3 Results

Neutrons

The induced attenuation in the fibres is presented in Figure 6-6a, along with the result of a test performed by others on the POF fibre at a reactor facility in Ljubljana [4]. Since manual test methods were used to measure the induced attenuation for the POF fibre, there are significant errors due to variations in coupling efficiencies as fibre connectors are manipulated during the course of the test. None–the–less the POF fibre is clearly more radiation tolerant than the Acome–supplied fibre. At the neutron fluence expected for the calorimeter links, the induced attenuation for the POF fibre is approximately 0.07 dB/m. Extrapolating the Acome result to such fluences yields an induced attenuation in excess of 0.3 dB/m. Figure 6-6c is shows the light power output for the Acome fibre during and after the neutron irradiation as a function of time. The fibre immediately starts to anneal after the end of the irradiation and regains about 1/3 of the light power lost during the neutron exposure.

Induced Attenuation

The induced attenuation per meter of the fibre is defined as:

$$\frac{20 \cdot \log(P_1/P_2)}{l} \text{ dB/m}$$

where l is the length of the fibre and P_1 and P_2 is the light power measured before and after the irradiation.

Gamma

The induced attenuation in the Acome–supplied fibres is shown in Figure 6-6b, along with the result of four radiation tests of the POF fibres, performed by others [4]. It is immediately apparent from this figure that the Acome–supplied fibre is not applicable for use in ATLAS. Even for the modest radiation levels expected at the calorimeter, the induced attenuation ex-

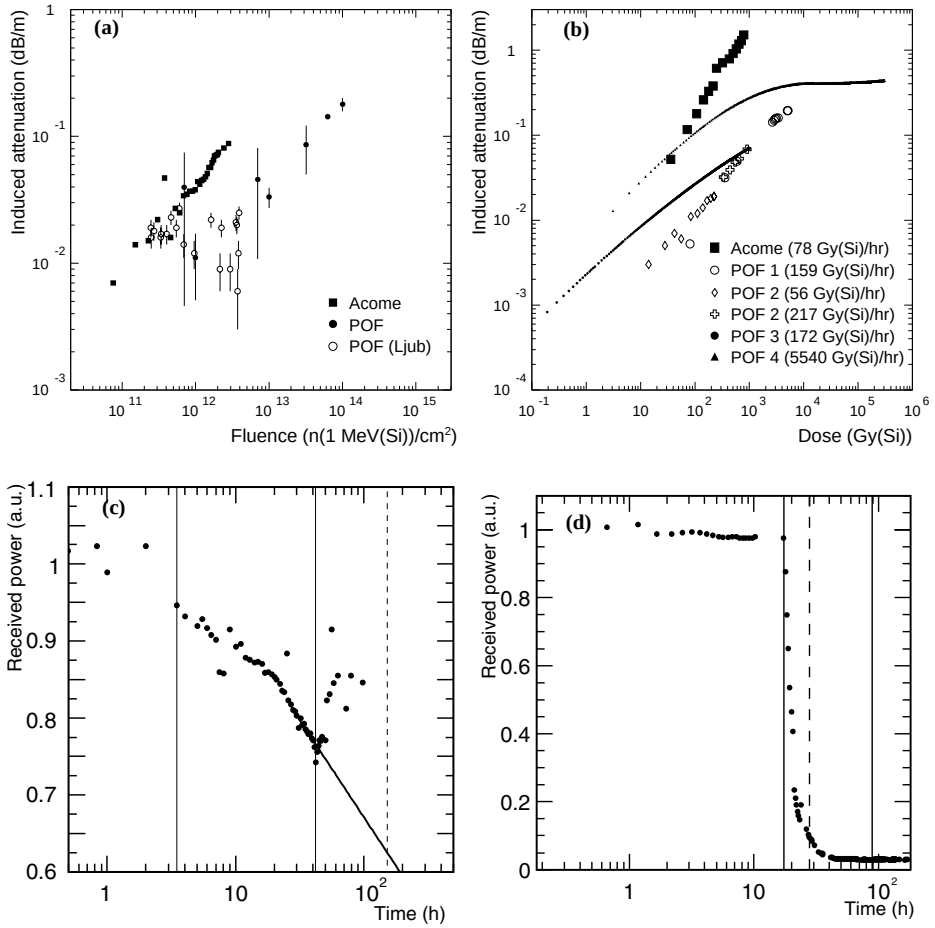

Figure 6-6:
a) The induced loss in the POF and Acome-supplied fibres as a function of neutron fluence. The POF(Ljub) measurements come from a test done by others [4]. For the POF fibres the points with the smaller error bars correspond to the longer length of fibre tested.
b) The induced loss in the POF and Acome–supplied fibres as a function of ionising dose. The POF measurements come from four independent tests done by others [4]
c) The light power throughput in an Acome fibre during exposure to neutron irradiation. After the end of the irradiation the fibre is seen to anneal.
d) The light power throughput in an Acome fibre during exposure to gamma irradiation. No evidence of annealing is seen after the end of the irradiation.

ceeds 1 dB/m. Figure 6-6d is shows the light power output for the Acome fibre during and after the gamma exposure as a function of time. No signs of annealing is seen.

6.5 Performance of the Transceivers

Transceivers from AMP, Hewlett Packard, Honeywell and Methode [50] were evaluated. All but the Methode transceiver died or became unstable during a 10 year equivalent neutron irradiation. For those devices that where possible to examine after the test, it was discovered

that the VCSEL was still operational but the driving circuitry had died. The gamma radiation tolerance of the transceivers has been tested and found to withstand up to a total dose of 800 Gy(Si).†

6.6 G–link Irradiation

6.6.1 Experimental Procedure

Functionality tests of 4 G–link Tx chip after they were exposed to neutron and gamma were performed. A Bit Error Rate (BER) test for a non irradiated G–link Tx chip was made prior to irradiation. The chips were then positioned in the radiation field and given doses of 5×10^{13}n(1MeV(Si))/cm^2 in the case of neutrons and 3kGy(Si) in the case of gamma, which corresponds to an equivalent dose of ~40 years LHC running (at high luminosity). After the irradiation the same BER test was performed to look for any difference in functionality.

6.6.2 Results

Neutrons

The neutron tests demonstrated that the G–link serialiser withstands the delivered neutron fluence. However, during the test single–event upsets were observed. This led to further experiments, which is the topic for the next chapter.

Gamma

The G–link chip was also found to withstand the delivered gamma dose. During this test a lead block was used to shield the rest if the components on the link transmitter board. As this test was done after the neutron irradiation where SEUs were observed to occur, this was also looked for, but no SEUs were seen.

–♦–

† This test was performed by colleagues at Southern Methodist University.

CHAPTER 7

SEU TESTS OF THE DEMONSTRATOR LINK

When performing the neutron total dose studies of the G–link, SEUs were observed. This behaviour required further testing. Three neutron irradiation tests of the demonstrator link were performed, one at SARA, one at CERI and one at Chalmers. The SEU rate dependence on flux and neutron energy was measured. The aim was to infer the SEU rate in ATLAS, by means of the BGR method discussed in Chapter 4. The results presented in this chapter are summarised in a paper submitted to Nucl. Instr. and Meth. A [5].

7.1 Experimental Procedure

7.1.1 General Description

An overview of the demonstrator link under test is shown in Chapter 4.4. In a typical irradiation test setup, illustrated in Figure 7-1, two link transmitter boards were exposed to neutron radiation at the SARA, CERI or Chalmers neutron facilities (see previous chapter for a description of these).

The ideal way of performing a SEU test of a device like the G–link is to use a bit error rate testing (BERT) system, which feeds a known data pattern to the transmitting end and compares it to the pattern appearing at the receiving end. Such a system is however very expensive and was not available when these tests were conducted. Instead the behaviour of the links was observed during irradiation, using a "poor man's BERT" according to the following scheme:

The links (running in double–frame mode†) transmitted either fill frames† or data fixed to FFFF. The latter was only done at tests performed at CERI. Errors were detected at the receiving end by using programmable logic (an ALTERA® Flex board [51]) connected to the receiver boards. The ALTERA board was programmed to register the following occurrences:

- the assertion of the G–link (Rx) ERROR–flag, indicating that a received frame does not correspond to either a valid data or Fill frame encoding.†
- the assertion of the G–link (Rx) LINKREADY–flag, indicating that the G–link start–up sequence is complete and that the data and control indications are valid.†

In the CERI test the following occurrence was added:

- any deviations from the fixed FFFF‡ data pattern.

The disappearance of the fixed FFFF pattern triggered the start of a 25 MHz counter which proceeded counting until the FFFF pattern was re–established. This arrangement had the advantage of providing information about the time–extension as well as the rate of the errors.

Each time any of the three occurrences happened, the information about the flag status as well as the counter value (only at CERI) was written into a register. The register was con-

† See Chapter 4.4 for a more detailed explanation.
‡ In retrospect a better choice would have been to use FF00 to test for both kinds of bit flips 1 to 0 and 0 to 1.

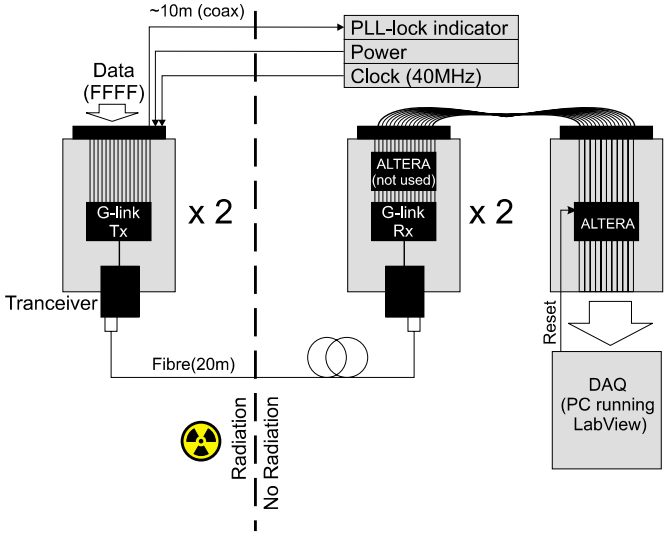

Figure 7-1: The demonstrator link in a typical test beam setup.

tinuously monitored by a data acquisition system, which was composed of a PCMCIA DAQ–card† inserted in a PC running LabView‡. Every time the value in the register deviated from zero the LabView program saved it to disk, and subsequently sent a reset signal back to the ALTERA, which reset the register to zero and continued looking for errors.

Coaxial cables (~10 m) for the clock signal, power and monitoring of the G–link Tx PLL–lock indicator was routed between the irradiated transmitting end of the link and the control room.

7.1.2 Radiation Environment

The error rate dependence on the neutron flux was demonstrated at the SARA facility by varying the intensity of the incident deuteron beam. The deuteron currents were 100, 200, 500, 1000 and 5000 nA. The irradiated components were placed ~30 cm from the target behind the liquid argon filled cryostat. The neutron flux at this position is derived from the neutron–yield curve in Figure 6-1b, assuming a $1/r^2$ decrease in neutron intensity and an attenuation of a factor 2 [41] in the cryostat. The flux levels are shown in Table 7-1. No check of the data field was performed at this test as only the two error flags were monitored.

At CERI, data were taken at the deuteron beam energies 5, 7, 14, 20 and 25 MeV. The choice of beam current for the different energies was made so that a nominal neutron flux of the order 3×10^7 n cm^{-2} s^{-1} was obtained (this is ~70 times higher the simulated total ATLAS flux at high LHC luminosity§). The neutron yield at different deuteron energies has been estimated using the curve in Figure 6-1b. Table 7-2 shows a summary of the radiation conditions during the test. The transmitting end of the link was placed 20 cm from the target.

† DAQ1200, manufactured by National Instruments.
‡ A data acquisition and instrument control software from National Instruments.
§ This choice of flux was estimated to be needed in order to make the statistical errors sufficiently small.

Beam Current [nA]	Flux (±15%) [$\times 10^7$ cm^{-2}·s^{-1}]
100	0.4
200	0.7
500	1.8
1000	3.6
5000	18

Table 7-1: A summary of the radiation conditions at the SARA test. The deuterium beam energy was fixed to 20 MeV. The 15% uncertainty in the flux comes from the Ni foil dosimetry.

Beam Energy [MeV]	Beam Current [nA]	Flux (±15%) [$\times 10^7$ cm^{-2}s^{-1}]
5	6200	3.0
7	5800	2.8
14	400	2,4
20	190	3,1
25	90	2,9

Table 7-2: A summary of the radiation conditions at the CERI test.The 15% uncertainty in the flux comes from the Ni foil dosimetry.

7.2 Results

7.2.1 Error Types

During neutron the irradiations, two types of errors were detected, single bit flips and longer errors where the G–link synchronisation was lost (indicated by the LINKREADY flag).

Short Errors (bit flips)

This type of error was first seen with an oscilloscope at SARA where the G–link ERROR flag was asserted for 12.5 ns, corresponding to one clock cycle of the 80 MHz clock used by G–link when running in double–frame mode. As discussed previously, the ERROR flag indicates that a received frame does not correspond to either a valid data, control or fill frame encoding. Therefore, this type of erratic behaviour is interpreted as if a neutron has caused a transient error with the result that a corruption of this encoding has occurred.

When the check for the integrity of the FFFF data was implemented in the CERI test, short bit flips where one of the bits (sometimes more) in the fixed FFFF pattern suddenly dropped to zero for 12.5 ns were also observed. The same ERROR flag corruption as seen at SARA was also seen. However, the data errors were dominant and the ratio between the two was about 20/3. In Figure 7-*i* on the next page a screen shot of a typical bit flip is shown.

Long Errors

The link was also observed to lose its synchronisation for periods as long as ~1 ms. During this link–down time the data was totally corrupted, and showed the behaviour illustrated in Figure 7-*ii*. This is interpreted as a neutron is effecting some part of the circuit that controls the G–link synchronisation mechanism. These errors always caused he assertion of the LINKREADY–flag. The time extension of these “link down errors”, and the ratio between the number of errors of this type and the other error types, has been seen to show substantial variation from test to test. This is believed to be an effect of different matching between the clock signals used by transmitter and receiver G–link [52]. In Figure 7-2 the distribution of link–down times measured at CERI is shown.

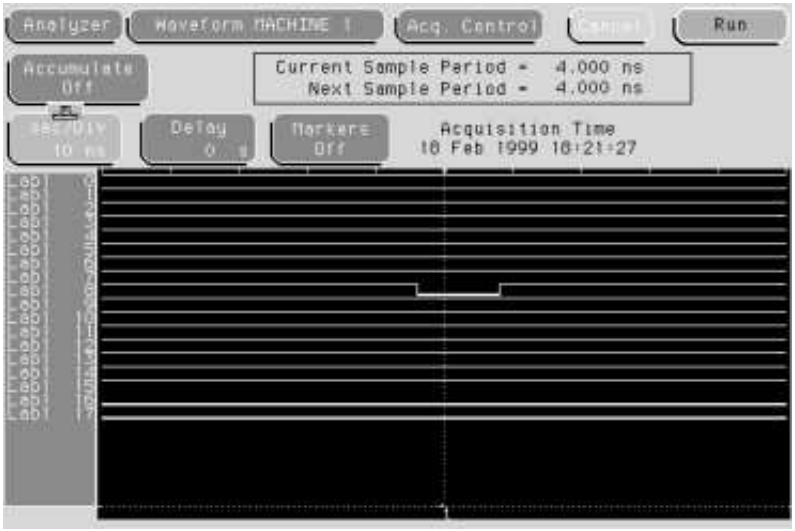

Figure 7-i: A logic analyser screen shot of a short bit flip in the 8'th data bit. The time extension of this error is 12.5 ns corresponding to one period of the 80MHz clock used by G–link when running in double frame mode.

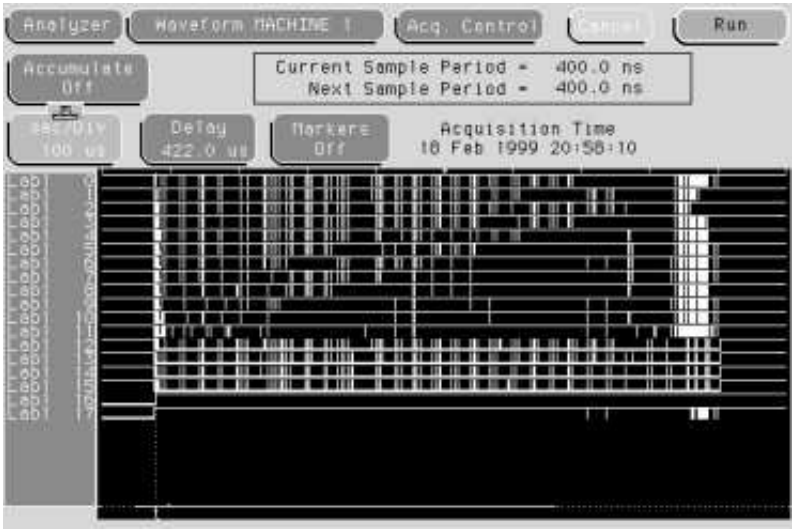

Figure 7-ii: A screen shot of the G–link data field during a long error when the link synchronisation is lost. This particular error is ~800µs long.

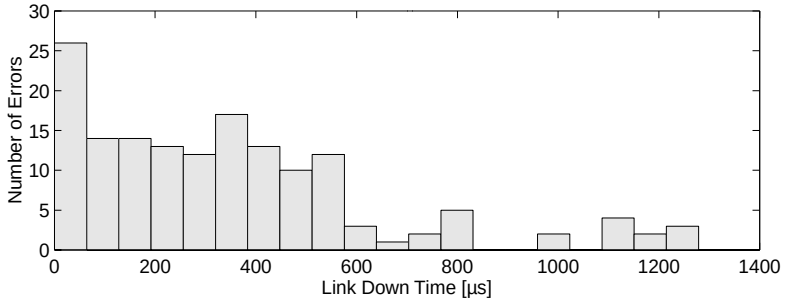

Figure 7-2: The distribution of link–down times measured at CERI.

7.2.2 Measured Error Rates

Neutrons

The test at SARA where the deuterium beam current was varied, but the energy was held fixed, showed a linear relation between the error rate and the beam current (and consequently the neutron flux). The measured error rate per link for the type of error where the G–link ERROR flag was asserted as a function of deuteron current is plotted in Figure 7-3.

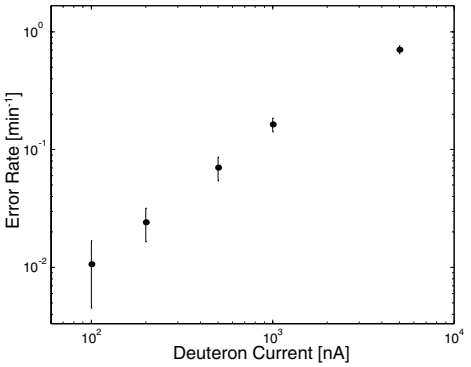

Figure 7-3: The measured error rate at a fixed deuteron beam energy (20MeV) as a function of the incident deuteron beam current (which is proportional to the neutron flux measured at SARA).

The test carried out at the Chalmers facility showed that 2.45MeV neutrons induce no errors of any kind, whilst 14.1MeV neutrons do. This result is in full agreement with the discussion in Chapter 5.5.2 which concluded that the nuclear processes responsible for generating neutron induced SEUs have a threshold at a neutron energy of about 5MeV. In Figure 7-4 the measured error rate at a fixed neutron flux is shown as a function of deuteron beam energy, measured at CERI. The figure shows that the error rate becomes larger as the beam energy is increased. The fraction of data, ERROR–flag and LINKREADY–flag errors is indicated in the figure. All error rates are for one link.

The dead time τ for the read out system was measured to be about 5ms. The true error rate then differs from the measured R_{SEU} by a factor $1/(1-\tau R_{SEU})$. This factor is around 1.0001 at the highest measured error rates. Thus, the probability of having an error during the time when the system was occupied with recording a previous one was negligible.

7.2.3 BGR Analysis

The neutron spectra produced by the 7, 14, 20 and 25 MeV deuteron beams hitting the beryllium target are plotted in Figure 6-2 [44]. From the discussion presented in Chapter 5.5.2 it is expected that the error rate increases when the neutron spectrum is shifted towards higher energies. From Equation 5-10, the predicted SEU rate for a specific neutron spectrum (labelled *spect*) is given by:

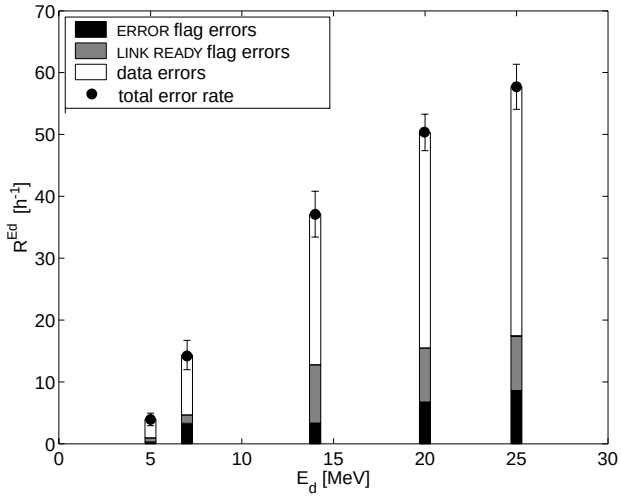

Figure 7-4: The measured error rate at a nominal flux of 3×10^7 $ncm^{-2}s^{-1}$, as a function of deuterium energy. The different shading indicates the fraction of the different error types: data, ERROR flag and LINK READY flag.

$$R_{\mathrm{SEU}}^{spect}(E_c) \;=\; \varepsilon V \times \int BGR(E_c)^{spect} \times \phi^{spect} \qquad (7\text{-}1)$$

For the ATLAS spectrum and any one of the five spectra from the SEU tests, the two following equations can be derived:

$$R_{\mathrm{SEU}}^{Ed}(E_c) \;=\; \varepsilon V \times \int BGR(E_c)^{Ed} \times \phi^{Ed} \qquad (7\text{-}2)$$

$$R_{\mathrm{SEU}}^{\mathrm{ATLAS}}(E_c) \;=\; \varepsilon V \times \int BGR(E_c)^{\mathrm{ATLAS}} \times \phi^{\mathrm{ATLAS}} \qquad (7\text{-}3)$$

Both equations are specific cases of Equation 7-1. However, in Equation 7-2 the error rate R^{Ed} has been directly measured for the five different E_d values (thus, Equation 7-2 is really five different equations, one for each value of E_d). This equation will be used to estimate E_c and εV. These values can be used in Equation 7-3 to estimate R^{ATLAS}. A convenient way to do this in "one step" is to eliminate the device specific factor εV from the two equations above, thus:

$$\underbrace{\frac{\phi^{\mathrm{ATLAS}}}{\phi^{\mathrm{Ed}}} \times R_{\mathrm{SEU}}^{Ed}}_{Y(E_d)} \;=\; R_{\mathrm{SEU}}^{\mathrm{ATLAS}} \times \underbrace{\frac{\int BGR(E_c)^{Ed}}{\int BGR(E_c)^{\mathrm{ATLAS}}}}_{X(E_d,\,E_c)} \qquad (7\text{-}4)$$

The left hand side of this equation, $Y(E_\mathrm{d})$, is simply the measured error rate, at a specific deuterium energy and, normalised to the total neutron flux in ATLAS. The first factor on the right hand side is the sought ATLAS error rate, and the second factor, $X(E_\mathrm{d},E_\mathrm{c})$, is the ratio between the BGR convolution integrals (Equation 5-9) for the ATLAS spectrum and the spectra from the various deuterium energies. This factor depends on the value of E_c. It is therefore hypothesised is that R^{Ed} is proportional to BGR(E_c). This is tested by a linear

χ^2–fit between $X(E_d,E_c)$ and $Y(E_d)$. There are five different measurements of R^{Ed} for five different neutron spectra, therefore the number of degrees of freedom in the fit is 3 (there

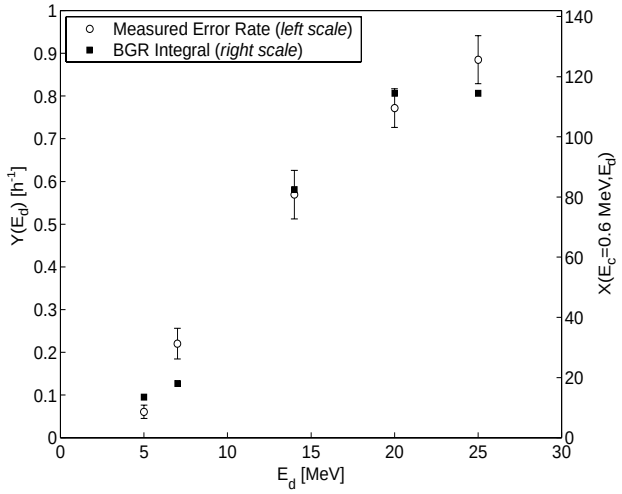

Figure 7-5: The transient error rate overlaid with the BGR convolution integrals.

are 2 free parameters, R^{ATLAS} and E_c).

When including all three types of errors, a minimal χ^2 value was obtained for E_c=0.64 MeV corresponding to a R^{ATLAS} value of 0.007 h^{-1}. The uncertainty in E_c is then estimated by taking the values that are given one sigma below and above the minimum χ^2. Table 7-3 shows a summary of these results. In Figure 7-5, the left hand side and the right hand side of Equation 7-4 has been plotted for E_c=0.64 MeV. Hence, the total ATLAS error rate is estimated to be 0.007±0.002 h^{-1}. This result does not include any uncertainties in the knowledge

	χ^2**(3 d.o.f)**	E_C **[MeV]**	R^{ATLAS} **[h^{-1}]**
$+1\sigma$	4.7	0.85	0.0087
mean	3,7	0.64	0.0074
-1σ	4.7	0.43	0.0064

Table 7-3: Summary of the fit–result.

of the actual neutron flux for each deuterium energy. If a 15% uncertainty (due to the uncertainty in the Ni foil analysis) is taken account for the result becomes 0.007±0.003 h^{-1} with a minimum χ^2 of 2.9 (3 d.o.f.).

Since the result is directly proportional to the simulated ATLAS flux. The quality of the simulations are of course crucial to the result. The model discussed above has however shown to be rather insensitive to the shape of the ATLAS spectrum as long as the fraction of neutrons with energies above the threshold for generating SEUs (~5 MeV) doesn't change significantly. If for some reason new simulations indicate that this is no longer true the ATLAS error rate will have to be re estimated. With a safety factor of 3, which has been proposed [53], the error rate could be as large as 0.02±0.01 h^{-1}. That means between 1and 3 errors every 100 hour.

CHAPTER 8

SUMMARY AND OUTLOOK

8.1 Total Dose Studies of Single Components

8.1.1 VCSELs

The light output of VCSELs are attenuated by neutron irradiation due to atomic displacements in the GaAs. The measured attenuation was 5–10% for the fluence equivalent of 10 years of LHC running. The devices were biased above lasing threshold during irradiation. After the end of the irradiation measurements continued for 90 hours. Annealing behaviour was seen where the VCSELs light output was returned to ~95% of their initial value.

Gamma irradiation up to a dose equivalent of 10 years of LHC running, had a negligible effect on the glass window or lens in the VCSEL TO–46 package. At the end of the irradiation period (equivalent of ~65 years of LHC running) an attenuation of ~15% was seen for all VCSELs. No annealing recovery occurred afterwards.

The attenuation in the light output of the VCSELs is small and will not present a problem for the optical power budgets envisaged for the read-out links of the ATLAS liquid argon calorimeter.

8.1.2 Fibres

Two different fibres, one from Acome and one from Plasma Optical Fibres (POF), were irradiated. The Acome fibre was irradiated with both neutrons and gamma radiation and showed an attenuation of 0.3dB/m and ~1dB/m respectively for a neutron fluence and ionising dose equivalent of 10 years of LHC running†. After the neutron test the fibre were seen to anneal and the light power throughput returned to ~85% of its initial value. The POF fibre was only irradiated with neutrons and was found to attenuate by 0.07dB/m after a 10 year equivalent fluence.

The induced attenuation of ~1dB/m shown by the Acome fibre during gamma irradiation, would have a serious impact on the optical power budget of the links. Therefore this fibre is not sufficiently radiation tolerant for use in ATLAS. This is thought to be due to the phosphorous doping in the fibre core. The POF fibre on the other hand is suitable for use at the position of the LAr links.

8.1.3 Transceivers

A transceiver from Methode was found to withstand a neutron fluence equivalent of 10 years LHC running.

As only one port of the transceiver is used at either end of the link, this solution may prove to be too costly for ATLAS. The identification of a radiation tolerant VCSEL driver is a priority to allow migration away from transceivers.

---

† The neutron result was extrapolated from the fluence 3×10^{12}n(1MeV(Si)/cm^2), delivered at the test.

8.1.4 G–link Serialiser

The G–link was found to function correctly after being irradiated with 3kGy(Si) ionising radiation and 5×10^{13}n(1MeV(Si))/cm^2, and could from this point of view be considered as the serialiser of choice for the LAr optical links. However Single Event Upsets (SEUs) were seen !

8.2 SEU Studies of the G–link

The G–link transmitter chip was seen to exhibit SEUs. Two types of errors were seen *i)* single 12.5ns bit flips in the transferred data and of the G–link error flag and *ii)* longer errors where the link synchronisation was lost for typically a period of hundreds of µs. A method based on the use of BGR curves was used to determine the error rate in ATLAS like radiation conditions was developed during the course of this work. With a safety factor of 3, the total ATLAS error rate is estimated to be 2±1 errors per 100h.

In a scenario where a whole ATLAS event would have to be rejected every time a single link gives an error of any kind, and accounting for 1620 LAr links, the event rejection rate becomes ~50h^{-1}. This is very small compared to the 270 000 events accepted by the LVL1 trigger every hour. However, in order to re–synchronise the ROD after a “link down” error a reset will need to be issued. The exact implementation of this is not yet defined but could take a significant amount of time which means that the effective event loss will be to large.

Table 8-1 summarises the results of all the measurements.

Type of Studie	Component	Particle Type	Type of Damage	Measured Effect	Value	Annealing (% of initial value)
Total Dose	VCSELs+ Packages	Neutrons	Displacement	VCSEL attenuation	5-10%[a]	Yes (95%)
		Gamma	Ionising	Lens attenuation	<5%[a]	No
	Fibre (POF)	Neutrons	Secondary Ionisation	Attenuation	0.07dB/m[a]	Yes (85%)
	Fibre (Acome)	Neutrons	Secondary Ionisation	Attenuation	0.3dB/m[a]	Yes (85%)
		Gamma	Ionising	Attenuation	~1dB/m[a]	No
	G–link	Neutrons	Displacement	None	–	–
SEU	G–link	Neutrons	Secondary Ionisation	SEUs seen	3±1error/100h[b]	–
	G–link	Gamma	Ionisation	No SEUs seen	–	–

Table 8-1:

a. for 10 yrs of LHC running.
b. all types of errors included.

8.3 Outlook

The work detailed in this thesis has shown that it is feasible to construct an optical link based on novel surface emitting lasers and multimode fibres which has sufficient total dose tolerance for use in the read–out of the LAr calorimeter systems. At this time it is not possible to predict whether the SEU rate due to the serialiser will have a significant effect on the integrity of the overall LAr read–out system. With this in mind, attention has recently been focused on the development of truly error free optical links. The logical extension to the single G–link solution explored in this thesis is to use a technique whereby data is sent from each FEB on two identical optical links [54]. A fast error checking and switching system is implemented at the receiver to ensure error free transmission of data to the RODs. This system

is only feasible given the modest predicted link SEU rate. Another possibility is the use of high speed (2.5Gb/s) GaAs serialisers and deserialisers which are now becoming commercially available and are expected to be radiation tolerant [54].

–♦–

CHAPTER 9

ACKNOWLEDGEMENTS

First of all I would like to thank Prof. Per Carlson for taking me on as a Ph. D. student in the group three years ago. The work with the optical link which I immediately became involved with was lead by Mark Pearce from whom I've learnt a lot and also become good friend with ("I suppose") during these years. I also want to thank Bengt Lund–Jensen who is the head of the ATLAS section of the group and also my supervisor. He always has an answer to every question.

Other people I've had a good time working with during this period is our electronic engineer Stefan Rydström and the optical link working group; Marie–Laure Andrieux (ISN), Bernard Dinkespiler (CPPM/SMU) and Ryszard Stroynowski (SMU) with whom I have spent some intense hours when doing the various radiation tests. Thanks also to Christophe Clément who has helped me several times with my analysis, and to Jesper Söderqvist the "father" of all Ph. D. students in the ATLAS group for building a good foundation for the rest of us.

The well–ordered arrangements when performing the irradiation tests at Karolinska and at Chalmers were thanks to Bengt Inge Rudén and Imre Pázsit.

I've also had the pleasure of sharing my office with a very nice person called Linda Megner who started as a student in the group just after me. By combining bravery (Linda) and afterthought (me) we make an excellent team when calculating exercises for the courses we often take together. Another person that I'm very glad to meet every morning I come to the office is Theresa Lamroth who I promise to talk a lot more to now than I've done these last weeks.

Thanks also to Awatif Belyman, Mats Lundqvist, Björn Cederström, Jens Lund, David Bergström, Mirko Boezio, Janina Östling, Monica Wallmark, Patricia Hansen, Leif Ericsson, Tom Francke, Oana Boezio and for being good friends and colleagues.

–♦–

Bibliography

[1] W. C. Röntgen, *Über eine neue Art von Strahlen*, Sitzungsberichte der Physikalisch-medizinischen Gesellschaft zu Würzburg. Vol.137 (1895)

[2] J.T. Wallmark, S.M. Marcus, *Minimum Size and Maximum Packing Density of Nonredundant Semiconductor Devices*, Proc. IRE (286), 1962

[3] M,-L. Andrieux, et. al., *Neutron and Gamma Irradiation Studies of Packaged VCSEL Emitters for the Optical Read–Out of the ATLAS Electromagnetic Calorimeter*, Nucl. Meth. Instr. A 426 332 (1999)

[4] G. Mahout et al., *Irradiation Studies of Multimode Optical Fibres for use in ATLAS Front-end Links*, ATL-ELEC-99-001, (Accepted for publication in NIMA 16th November 1999)

[5] M.-L. Andrieux et al., *Single Event Upset Studies of a High Speed Digital Optical Data Link*, ATL-LARG-2000-003

[6] LHC Collaboration, *The LHC Conceptual Design Report - The Yellow Book*, CERN/AC/95-05(LHC)

[7] J. Pinfold and P. Sinervo, *The TeV Physics Frontier: Probing the Microcosm*, Physics in Canada, v.50, no.2, p. 175-189, march/april, 1994

[8] CMS Collaboration, *The Compact Muon Solenoid, Technical Proposal*, CERN/LHCC/94-38 LHCC/P1, 15 December 1994

[9] LHC-b Collaboration, *LHC-b Technical Proposal*, CERN/LHCC/98-4, 20 February 1998

[10] ALICE Collaboration, *Technical Proposal for A Large Ion Collider Experiment at the CERN LHC*, CERN/LHCC/95-71, 20 December 1995

[11] ATLAS Collaboration, *ATLAS Technical Proposal*, CERN/LHCC/94–43 (1994)

[12] S.L. Glashow, *Partial Symmetries of Weak Interaction*, Nucl. Phys. 22 1031 (1961)

[13] A. Ferrari, et al., *Radiation Calculations for the ATLAS Detector and Experiment Hall, 2nd Workshop on Simulating Accelerator Radiation Environments*, 1997 CERN-TIS-RP-97-05 (48-60)

[14] ATLAS Collaboration, *ATLAS Inner Detector Technical Design Report volume 1*, CERN/LHCC/97-16 ATLAS TDR4 (1997)

[15] ATLAS Collaboration, *ATLAS Tile Calorimeter Technical Design Report*, CERN/LHCC/96-24 ATLAS TDR4 (1996)

[16] ATLAS Collaboration, *ATLAS Muon Spectrometer Technical Design Report*, CERN/LHCC/97-22 ATLAS TDR10 (1997)

[17] ATLAS Collaboration, *ATLAS Level-1 Trigger Technical Design Report*, ATLAS TDR12 (1998)

[18] ATLAS Collaboration, *ATLAS Liquid Argon Calorimeter Technical Design Report*, CERN/LHCC/96-41 ATLAS TDR2, 15 December (1996)

[19] ATLAS Collaboration, *ATLAS Detector and Physics Performance Technical Design Report*, CERN/LHCC/99-14 ATLAS TDR14, 25 May (1999)

[20] J. Dowell and M. Pearce, *ATLAS Front-end Read-out Link Requirements*, ATLAS Internal Note ATLAS-ELEC-98-001 15 th July 1998

[21] M. Dentan, et. al., *Final Acceptance of the DMILL Technology Stabalized at TEMIC/MHS*, LEB Rome CERN/LHCC/98-36 30 October 1998

[22] Jim Tatum et al., *High Speed Characteristics of VCSELs*, Honeywell's MICRO SWITCH Division

[23] J. Söderqvist et al., *Radiation Hardness Evaluation of an Analogue Optical Link for Operation at Cryogenic Temperature,*, IEEE Trans. Nucl. Sci. 44 (1997) 861

[24] J. Gower, Optical Commuications System, Prntice-Hall inc., ISBN 0-13-638056-5

[25] *Vertical Cavity Surface Emitting Laser Devices*, Springer Verlag, Herbert Li Editor (in print)

[26] P.E. Green, Jr. Fiber Optic Networks, Prentice-Hall, Inc. ISBN 0-13-319492-2, 1993

Bibliography

[27] G–link Technical Data sheet, *Low Cost Gigabit RateTransmit/Receive Chip Set with TTL I/Os*

[28] F.W. Bopp et al., Phys Rev. D49 (1994) 3236; P. Aurenche et al., Phys Rev. D45 (1992) 92

[29] A. Ferrari, P.R. Sala, G. Guaraldi, and P. Padoani, Nucl. Instr. and Meth. B71 (1992) 412

[30] T.A.Gabriel and C.Zeitnitz, *The GEANT-CALOR Interface User's Guide*, GCALOR Version 1.04/10

[31] J.R. Srour and J.M. McGarrity, *Radiation Effects on Microelectronics in Space*, Proceedings of the IEEE, vol. 76, No 11, November 1988

[32] E.J. Friebele et al., Nucl. Instr. and Meth. B1 (1984) 355

[33] E.J. Friebele et al., Appl. Opt. 19 (1980) 2910. and Appl. Opt. 21 (1982) 547

[34] A. Holmes and L. Adams, *Handbook of Radiation Effects*, Oxford Sci. Publ., ISBN 0-19-856347-7

[35] R.S. Wagner et al*., Transient measurements of ultra fast charge collection in semiconductor diodes*, IEEE Trans. Nucl. Sci., vol.34 (1240) 1987

[36] J.F. Ziegler and W.A. Lanford, *Effects of Cosmic Rays on Computer Memories*, Sience (776), 16 November 1979

[37] K.C. Chandler and T.W. Armstrong, *Operation Instruction for the High Energy Nucleon-Meson Transport Code, HETC*, Report ORNL-4744, Oak Ridge National Lab

[38] E. Normand and W. R. Doherty*, Incorporation of ENDF-V Neuton Creoss Section Data for Calculating Neutron-Induced Single Event Upsets*, IEEE Trans. Nucl. Sci. vol.36 NO.6 (2349) December 1989

[39] E. Normand, *Extensions of Burst Generation Rate Method for Wider Application to Proton/Neutron-Induced Single Event Effets*, Boeing Information, Space & Defence Systems, Seattle WA 9812-2499

[40] J. Collot et al., Nucl. Instr. and Meth. A350 (1994) 525

[41] Private communication with the SARA operational team

[42] P.J. Griffin et al., *The Role of Thermal and Fission Neutrons in Reactor Neutron–-Induced Upsets in Commercial SRAMs*, IEEE Trans. Nucl. Sci. vol.44 NO.6 (2079) December 1997

[43] Private communication with Gudmar Grosshög, Dep. of Reactor Physics, Chalmers University of Technology

[44] P. Grand and N.A. Goland, *An Intense Neutron Source Based Upon the Deuteron–Stripping Reaction*, NIM 145 (49-76), 1977

[45] Honeywell, *http://www.honeywell.com*

[46] Mitel, *http://www.mitel.com*

[47] L.-O. Eek et al. Development and Performance of a Receiver for an Analogue Optical Link, ATL-LARG-97-079

[48] Oslo Optical Cable. Acome, Mortain, France

[49] Plasma Optical Fiber BV., Eindhoven, Netherlands

[50] Methode Electronics Inc., Chicago, USA. *http://www.methode.com/*

[51] Altera, *http://www.altera.com,* University program

[52] Private comunication with T. Church, Honeywell

[53] Ph. Farthouat et al., ATLAS policy on Radiation Tolerant Electronics, ATLAS internal note ELEC-no-003 (1997)

[54] B. Dinkespiler et. al.,*Redundancy or GaAs ? Two Different Approaches to solve the Problem of SEU (Single Event Upset) in a Digital Optical link*, Submitted to LEB 2000

[55] R. Fernow, *Introduction to Experimental Particle Physics*, Cambridge University Press, ISBN 0521379407